The Astrophysical Journal, 710:1205–1227, 2010 February 20 doi:10.1088/0004-637X/710/2/1205

THE *CHANDRA* VIEW OF NEARBY X-SHAPED RADIO GALAXIES

Edmund J. Hodges-Kluck[1], Christopher S. Reynolds[1], Chi C. Cheung[2,3], and M. Coleman Miller[1]
[1] Department of Astronomy, University of Maryland, College Park, MD 20742-2421, USA
[2] NASA Goddard Space Flight Center, Code 661, Greenbelt, MD 20771, USA
Received 2009 July 7; accepted 2009 December 16; published 2010 January 28

ABSTRACT

We present new and archival *Chandra X-ray Observatory* observations of X-shaped radio galaxies (XRGs) within $z \sim 0.1$ alongside a comparison sample of normal double-lobed FR I and II radio galaxies. By fitting elliptical distributions to the observed diffuse hot X-ray emitting atmospheres (either the interstellar or intragroup medium), we find that the ellipticity and the position angle of the hot gas follow that of the stellar light distribution for radio galaxy hosts in general. Moreover, compared to the control sample, we find a strong tendency for X-shaped morphology to be associated with wings directed along the minor axis of the hot gas distribution. Taken at face value, this result favors the hydrodynamic backflow models for the formation of XRGs which naturally explain the geometry; the merger-induced rapid reorientation models make no obvious prediction about orientation.

Key words: galaxies: active – intergalactic medium

Online-only material: color figures

1. INTRODUCTION

"Winged" and X-shaped radio galaxies (XRGs) are centrosymmetric subclasses of Fanaroff–Riley (FR) type I and II radio galaxies (Fanaroff & Riley 1974) which exhibit a second, fainter pair of wings lacking terminal hot spots in addition to the symmetric double lobe structure seen in ordinary FR II galaxies (Leahy & Williams 1984). These galaxies comprise up to 10% of radio galaxies, although the galaxies in which the length of the wings exceeds 80% of that of the primary lobes ("classical" XRGs) are a very small subset of radio galaxies (Leahy & Parma 1992; Cheung 2007). The primary lobes of these galaxies, as in other radio galaxies, are produced by a jet emanating from an active galactic nucleus (AGN) which becomes decollimated as it propagates into and interacts with the surrounding medium. In FR II radio galaxies, the terminal shock where the jet rams into its environment is characterized by a radio hot spot (also often seen in the X-ray band, e.g., Hardcastle et al. 2004) which produces the so-called edge-brightened morphology. The absence of these hot spots in the fainter wings of XRGs implies that they do not harbor an active jet, although Lal & Rao (2007) argue in favor of a dual-AGN origin in which the pairs of lobes emanate from separate, unresolved AGN.

The X-shaped morphology is of interest because two remarkably disparate classes of models have been invoked to explain it. The first class is predicated on the reorientation of the jets either by realignment of the supermassive black hole (SMBH) spin or the accretion disk, whereas the second purports to explain the distorted morphology as the result of hydrodynamic interaction between the radio lobe and its surrounding gaseous environment on kiloparsec scales.

In the first case, the most common explanation for the X-shaped morphology is that the SMBH has its spin axis realigned, either via merger or precession. The possibility that XRG morphology is produced by a SMBH merger is of considerable interest as a potential estimate of merger rates and hence source rates for the *Laser Interferometer Space Antenna*; because fossil lobes will quickly decay due to adiabatic expansion, an XRG would be a sign of a recent merger. In this scenario (e.g., Rottmann 2001; Zier & Biermann 2001; Merritt & Ekers 2002), a SMBH binary formed by galactic merger and dynamical friction hardens for an unknown length of time via three-body interactions until gravitational radiation becomes effective at radiating orbital energy. At this point, the binary quickly coalesces, and the radio jets realign along the direction of the angular momentum of the final merged black hole. The jet begins propagating in the new direction, leaving a decaying pair of radio lobes along the old spin axis. A significant objection to the merger model (Bogdanović et al. 2007) is that the linear momentum "kick" imparted to the coalesced SMBH can exceed several times 10^3 km s^{-1} if the spins of the black holes are random at the time of merger, sufficient to escape the galaxy. Co-aligned spins reduce the magnitude of the kick, but would not result in an X-shaped source. Although not a problem for rapid reorientation models which rely on precession or other realigning mechanisms (Ekers et al. 1978; Rees 1978; Klein et al. 1995; Dennett-Thorpe et al. 2002), an additional objection to the "fossil" lobe scenario is that the secondary lobe lengths in some XRGs are inconsistent with the fast lobe decay expected when a jet changes alignment (Saripalli & Subrahmanyan 2009, hereafter S09).

In contrast to the rapid-realignment models, hydrodynamic models propose that the wings of XRGs were never directly inflated by a jet. These models argue that XRGs form due to backflow (plasma flowing back toward the AGN from the hot spot shocks) that interacts with the surrounding gas. As presently conceived, backflow models require FR II morphology to drive the strong backflows. The existence of FR I XRGs challenges these hypotheses, but S09 argue that, since several of the FR I XRGs appear to be restarted AGN with inner FR II morphology, the FR I XRGs could have had edge-brightened morphology when the wings were inflated, implying an evolution of FR II to FR I sources (Cheung et al. 2009). In this paper, we consider the backflow models as a unified class. The two most prominent backflow scenarios include the "buoyant backflow" model (Leahy & Williams 1984; Worrall et al. 1995) and the "overpressured cocoon" model (Capetti et al. 2002,

[3] Current address: National Research Council Research Associate, Space Science Division, Naval Research Laboratory, Washington, DC 20375, USA.

hereafter C02). The buoyant backflow model supposes that the buoyancy of the relativistic plasma cocoon in the interstellar or intragroup/intracluster medium (ISM or IGM/ICM) produces the additional wings. Because of the collimation seen in the more dramatic XRG wings, we refer to them hereafter as "secondary lobes" even though, if the hydrodynamic premise is correct, they are not of the same character as the primary lobes.

C02 propose a variant model in which backflowing plasma confined by an envelope of hot gas continues to aggregate until the cocoon of radio plasma is significantly overpressured, at which point it blows out of the confining medium at its weakest point. Supposing that the confining medium is the ISM of an elliptical galaxy, if the jet is aligned along the *major* axis of the galaxy, then the cocoon may become overpressured before the jet bores through the ISM, and the radio plasma will blow out along the *minor* axis of the galaxy, forming the secondary lobes. Conversely, if the jet is oriented along the minor axis of the galaxy, then backflow will either escape along the same axis or the jet will escape the ISM before the cocoon can become overpressured. C02 cite an intriguing correlation between the orientation of the secondary lobes in XRGs and the minor axis of the host galaxy as evidence for their model, which they further support with two-dimensional hydrodynamic simulations. In a follow-up study including "normal" radio galaxies, S09 find that the primary lobes of giant radio galaxies are preferentially aligned along the minor axis of the host, whereas they extend the original C02 result to a larger XRG sample. Although the observed geometric correlation is strong, much of the potentially relevant physics is absent in the C02 simulations, and Kraft et al. (2005) note that the buoyant backflow model can explain the observed correlation by assuming an anisotropic medium to divert the backflow. Moreover, it is unclear whether real radio lobes are actually overpressured. Reynolds et al. (2001) argue that an overpressured cocoon is inflated early on, but in the buoyant backflow model, the secondary lobes are formed later. In either case, the geometric correlation favors a hydrodynamic origin for the secondary lobes in the absence of an explanation for a relationship between the angular momenta of two merging SMBHs and large-scale structure of the galaxy. For the remainder of this paper, we refer to the "C02 geometry" to describe the correlation noted in XRGs and the proposed geometry of jet alignment that would produce them.

There are additional XRG formation models which are similar to the ones presented above in that they rely solely on either the black hole(s) involved or jet–gas interaction. These include the hypothesis that X- and Z-shaped distortions arise via gravitational interaction with another galaxy (Wirth et al. 1982; van Breugel et al. 1983), the idea that the jets are diverted by the ISM of a smaller merging galaxy (Gopal-Krishna et al. 2003; Zier 2005), and the aforementioned Lal & Rao (2007) proposal that both lobes are powered by active jets. Because these models are not as easily probed by the hot gas, we focus on the backflow models hereafter.

In this paper, we seek to characterize the properties of the hot gas in these systems and determine whether the C02 optical–radio geometric correlation also exists in the X-ray band. One assumption of the C02 proposal is that the stellar distribution traces the hot gas which makes up the confining medium. We will test this assumption directly by determining the extent to which optical and X-ray morphology are correlated. As a parallel study, we present the results from new and archival *Chandra X-ray Observatory* observations of XRGs and investigate whether the hot gas in XRG systems differs from that in a comparison sample of archival *Chandra* observations of "normal" FR I and II galaxies (taken largely from the 3CRR catalog; Laing et al. 1983).

Any observational study of XRGs is necessarily limited by the small number of known and candidate sources. Our study is further limited by two important factors: (1) the hot gas surrounding radio galaxies becomes increasingly difficult to characterize at higher redshift and (2) useful X-ray data do not exist for most XRGs. These considerations strongly constrain our conclusions. We therefore discuss in detail our target selection criteria in Section 2, as well as the observational parameters and reduction techniques applied to the data. In Section 3, we discuss our primary analysis of the morphology of the hot gas, and in Section 4 we discuss the X-ray spectra of the AGN. In Section 5, we summarize our results and interpretations.

Throughout this paper, we adopt the *Wilkinson Microwave Anisotropy Probe* (*WMAP*) values of $H_0 = 71$ km s^{-1} Mpc^{-1}, $\Omega_M = 0.27$, and $\Omega_{\rm vac} = 0.73$ with flat geometry. We calculate equivalent angular scale and distances at redshift using the online calculator provided by Wright (2006), and for Galactic absorption, we use the online HEASARC $N_{\rm H}$ calculator with values from the Leiden/Argentine/Bonn survey (Kalberla et al. 2005).[4]

2. *CHANDRA* OBSERVATIONS

Chandra is well suited to a study of the hot environments of radio galaxies thanks to its high sensitivity, 0.″5 spatial resolution, and 0.3–10 keV bandwidth. *Chandra* has also been able to resolve X-ray emission associated with the radio lobes into hot spots and jets (Hardcastle et al. 2004); distinguishing this emission from the gaseous halos is especially important for our purposes.

Our analysis sample of *Chandra* data consists of 18 comparison sample galaxies and 8 XRGs (Figures 1 and 2 with observational parameters in Table 1). In this section, we describe how we arrived at this sample, starting with the preliminary selection criteria for the XRG and comparison samples from radio data and availability in the *Chandra* archive (Section 2.1). After reducing these data, we rejected a number of galaxies due to low quality or pileup (Section 2.2), then used spectral fitting to find those galaxies where the diffuse gas dominates the photon count in the relevant regions (Section 2.3). These are the galaxies we include in our final sample (Table 1); Figures 1 and 2 are discussed along with the radio and optical data we use in Section 2.4.

We note that many of the archival data sets have been published, and references are provided in Table 1 where available. Our goal is not to exhaustively study any individual source. Notes on individual sources are found in the Appendix.

2.1. Preliminary Target Selection

The most complete compilation of known and candidate X-shaped sources in the literature is that of Cheung (2007), who used the NRAO[5] Very Large Array (VLA; Thompson et al. 1980) Faint Images of the Radio Sky at Twenty cm (FIRST; Becker et al. 1995) data to identify the candidate XRGs. For this paper, we define XRGs as comprising all radio galaxies in Cheung (2007) that have a wing length exceeding 80% of the

[4] See http://heasarc.gsfc.nasa.gov/cgi-bin/Tools/w3nh/w3nh.pl

[5] The National Radio Astronomy Observatory is a facility of the National Science Foundation operated under cooperative agreement by Associated Universities, Inc.

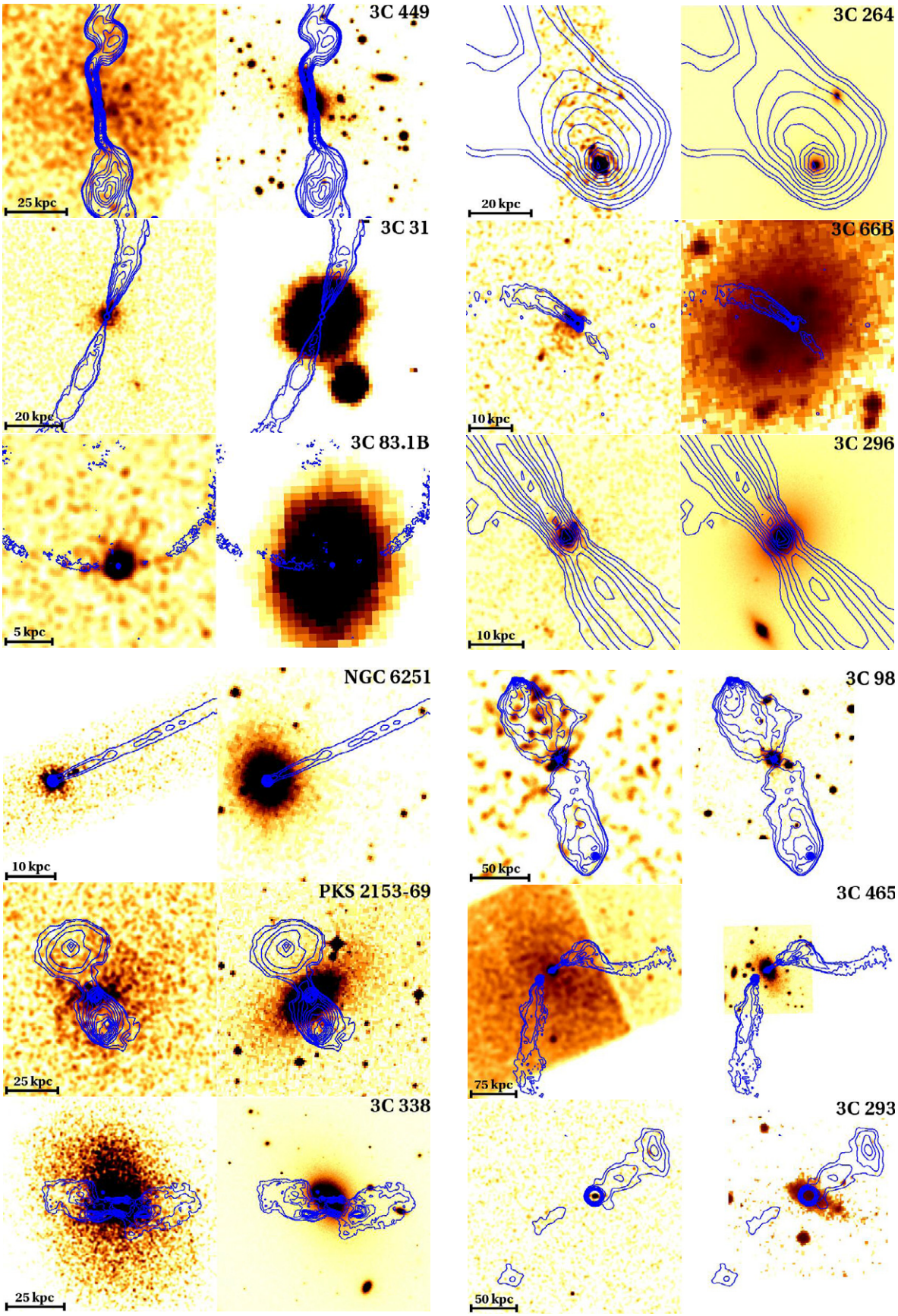

Figure 1. *Chandra* and optical images of our control sample galaxies with significant thermal emission. The left panel in each case is an image of the *Chandra* ACIS-S3 chip with uniform Gaussian smoothing and point sources removed. The right image is an optical image from DSS or SDSS. Overlaid in blue are VLA radio map contours. The images are sorted by ascending redshift. Note that for 3C 98 and 3C 388 the chip image is of the ACIS-I chip(s) instead of ACIS-S3.

(A color version of this figure is available in the online journal.)

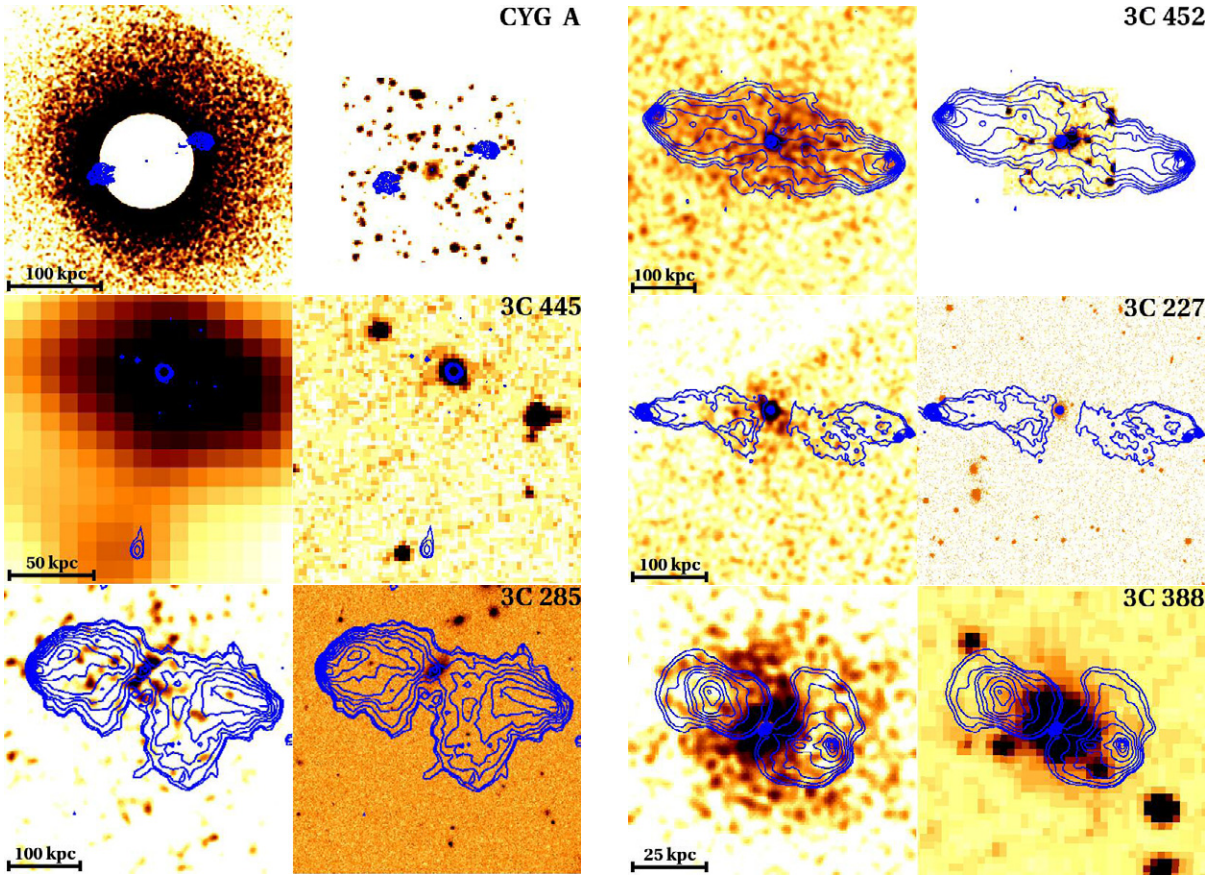

Figure 1. (Continued)

active lobes (Leahy & Parma 1992; the "classical" XRGS) and those "winged" sources in Cheung (2007) which have obvious X-shaped morphology in the angle between the active lobes and the wings. Assuming the projected lengths on the sky are the real lengths of the wings, in the backflow models these may be "classical" XRGs at an earlier stage.

We wish to study the hot gas surrounding the radio galaxy. The rapid decline in surface brightness and reduction in angular size with increased redshift makes a cutoff redshift of $z \sim 0.1$ practical for typical *Chandra* exposure times (even in this scheme, our sample is biased toward high pressure systems). Nineteen XRGs fall within this cutoff; the highest redshift in this group is $z = 0.108$. However, we have *Chandra* data for only 13 of these sources, and these comprise our preliminary sample. These sources include 3C 315, 3C 223.1, NGC 326, PKS 1422+26, 3C 433, 3C 403, 3C 192, B2 1040+31A, Abell 1145, 4C +00.58, 3C 136.1, 4C +32.25, and 4C +48.29.

This sample is heterogenous in its radio properties and morphology. A few of the galaxies may be described as Z-shaped (Gopal-Krishna et al. 2003; Zier 2005). NGC 326, for instance, has long secondary lobes that do not seem to meet at a common center. Others (e.g., B2 1040+31A) have obviously X-shaped lobe axes, but the lobes are not as well collimated as in NGC 326 or 3C 315. Lastly, PKS 1422+26, B2 1040+31A, and 3C 433 appear to be hybrid FR I/II radio galaxies with one FR I lobe and one FR II lobe (A "HYMOR;" see Gopal-Krishna & Wiita 2000). It is unknown whether these distinctions are signatures of any formation model, and we note that XRGs tend to lie close to the FR I/II break in other observables (Cheung et al. 2009).

In this paper, we use the definitions of Cheung (2007) and so consider the XRG sample as a unified whole, and we caution that our results are interpreted within this framework. In particular, there is no consensus in the literature on what constitutes an "X"-shaped galaxy. In their optical study, for example, S09 classify 3C 76.1 ($z = 0.032$) as an XRG, whereas we do not. They also classify several higher redshift galaxies as XRGs which do not appear in the Cheung (2007) list (e.g., 3C 401 or 3C 438); in this respect our sample is conservative. At least one high-redshift XRG from the Cheung (2007) list—3C 52 ($z = 0.285$)—has a *Chandra* exposure, and 3C 197.1 ($z = 0.128$) may be an XRG and is also in the *Chandra* archive. We choose not to use these exposures, although we note them in Appendix A.3.

Within the same redshift cutoff, we identify normal FR I and II galaxies in the *Chandra* archive as a comparison sample. The aim of this sample is to determine whether XRGs systematically differ in X-ray properties from normal radio galaxies. It is not obvious what constitutes an appropriate comparison sample because although FR II lobes are deemed necessary to produce X-shaped morphology in the backflow scenario, FR I XRGs exist (S09). In the S09 interpretation of FR I XRGs, the FR I lobes must have had FR II morphology at the time the wings were generated. Supposing that both the C02 model and S09 interpretation are correct, the "old" FR I lobes must obey the same geometry as their "active" FR II counterparts. A comparison of the XRG sample to both types is therefore useful. The combined sample also provides a larger reservoir of sources for measuring the correlation between optical and X-ray isophotes in the ISM. We adopt a preliminary comparison

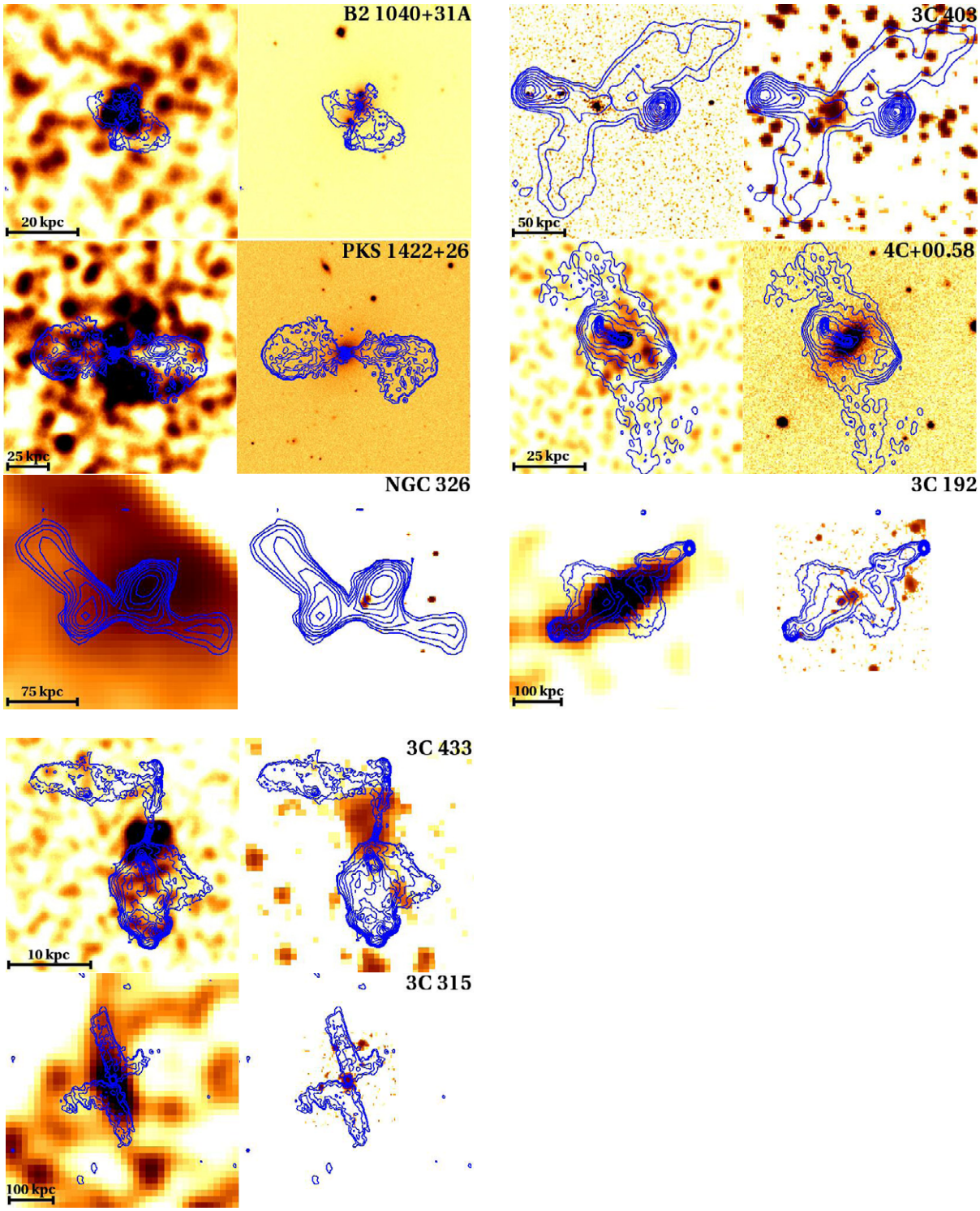

Figure 2. *Chandra* and optical images of our XRG sample galaxies with significant thermal emission. The left panel in each case is an image of the *Chandra* ACIS-S3 chip with uniform Gaussian smoothing and point sources removed. The right image is an optical image from DSS or SDSS. Overlaid in blue are VLA radio map contours. The images are sorted by ascending redshift.

(A color version of this figure is available in the online journal.)

sample consisting of (1) all FR II galaxies within $z \sim 0.1$ with data in the *Chandra* archive and (2) FR I galaxies from the DRAGN catalog[6] with the same conditions. There are 41 sources meeting these criteria.

2.2. Data Reduction

Thirteen XRGs and 41 normal radio galaxies comprise our preliminary samples, but the data for many of these are not of sufficient quality for our analysis. Both the archival data and our new data use Advanced CCD Imaging Spectrometer[7] (ACIS)

[6] Leahy, J.P., Bridle, A.H., & Strom, R.G., editors "An Atlas of DRAGNs" (http:/wwww/jb.man.ac.uk/atlas/).

[7] See http://cxc.harvard.edu/proposer/POG/pdf/ACIS.pdf.

Table 1
Chandra Observational Parameters

Name	Secondary Identifier	z	Ang. Scale (kpc/″)	Obs. IDs	Exp. Time (ks)	CCD Array	FR Type	Selected *Chandra* Refs.	Radio Refs.
				XRGs					
B2 1040+31A	J1043+3131	0.036	0.706	9272	10	ACIS-S	I/II	This work	AM221+AM222
PKS 1422+26	J1424+2637	0.037	0.725	3983	10	ACIS-S	I/II	This work	AM364
NGC 326	J0058+2651	0.048	0.928	6830	94	ACIS-S	I/II	1, 2, 9, 10	a
3C 403	J1952+0230	0.059	1.127	2968	49	ACIS-S	II	3, 4, 5	b
4C +00.58	J1606+0000	0.059	1.127	9274	10	ACIS-S	II	This work	AC818
3C 192	J0805+2409	0.060	1.144	9270	10	ACIS-S	II	6	c
3C 433	J2123+2504	0.102	1.855	7881	38	ACIS-S	I/II	7	b
3C 315	J1513+2607	0.108	1.951	9313	10	ACIS-S	I	This work	AM364
				Comparison sample					
3C 449	J2229+3921	0.017	0.341	4057	30	ACIS-S	I	4, 5, 8, 9, 10, 25	AK319
3C 31	J0107+3224	0.017	0.341	2147	45	ACIS-S	I	4, 5, 9, 11, 25	a
3C 83.1B	J0318+4151	0.018	0.361	3237	95	ACIS-S	I	4, 5, 12	AK403
3C 264	J1145+1936	0.021	0.419	4916	38	ACIS-S	I	4, 8	d
3C 66B	J0223+4259	0.022	0.439	828	45	ACIS-S	I	4, 5, 8, 13	e
3C 296	J1417+1048	0.024	0.477	3968	50	ACIS-S	I	4, 5	f
NGC 6251	J1632+8232	0.024	0.477	4130	50	ACIS-S	I/II	4, 14	g
PKS 2153−69	J2157−6941	0.028	0.554	1627	14	ACIS-S	II	15, 16	h
3C 338	J1628+3933	0.030	0.593	497+498	20+20	ACIS-S	I	4, 5, 8, 9, 14, 17	i
3C 98	J0358+1026	0.030	0.593	10234	32	ACIS-I	II	This work	j
3C 465	J2338+2702	0.031	0.612	4816	50	ACIS-S	I	4, 8, 9, 26	a
3C 293	J1352+3126	0.045	0.873	9310	8	ACIS-S	II	6	k
Cyg A	J1959+5044	0.056	1.073	360+5831	35+51	ACIS-S	II	18, 19	j
3C 445	J2223−0206	0.056	1.073	7869	46	ACIS-S	II	26	l
3C 285	J1321+4235	0.079	1.474	6911	40	ACIS-S	II	20	k
3C 452	J2245+3941	0.081	1.508	2195	81	ACIS-S	II	4, 21	b
3C 227	J0947+0725	0.087	1.609	6842+7265	30+20	ACIS-S	II	22	b
3C 388	J1844+4533	0.091	1.675	4756+5295	8+31	ACIS-I	II	23	m

Notes. Observational parameters for archival and proprietary *Chandra* data sets with significant thermal emission (see Table 3). Redshifts are obtained either from SIMBAD or compilation of Cheung (2007). X-ray references with more detail on the particular data set are provided above; not all references are provided. VLA program codes are provided where we processed data ourselves.

References. X-ray: (1) Worrall et al. 1995; (2) Murgia et al. 2001; (3) Kraft et al. 2005; (4) Evans et al. 2006; (5) Balmaverde et al. 2006; (6) Massaro et al. 2008; (7) Miller & Brandt 2009; (8) Donato et al. 2004; (9) Canosa et al. 1999; (10) Worrall & Birkinshaw 2000; (11) Jeltema et al. 2008; (12) Sun et al. 2005; (13) Hardcastle et al. 2001; (14) Evans et al. 2005; (15) Ly et al. 2005; (16) Young et al. 2005; (17) Johnstone et al. 2002; (18) Young et al. 2002; (19) Smith et al. 2002; (20) Hardcastle et al. 2007b; (21) Isobe et al. 2002; (22) Hardcastle et al. 2007a; (23) Kraft et al. 2006; (24) Sun et al. 2009; (25) Perlman et al. 2010; (26) Hardcastle et al. 2005.

Radio: (a) Condon et al. 1991; (b) Black et al. 1992; (c) Baum et al. 1988; (d) NRAO VLA Archive Survey; (e) Hardcastle et al. 1996; (f) Leahy & Perley 1991; (g) Sambruna et al. 2004; (h) Fosbury et al. 1998; (i) Ge & Owen 1994; (j) Perley et al. 1984; (k) Alexander & Leahy 1987; (l) Leahy et al. 1997; (m) Roettiger et al. 1994.

chips with no transmission grating in place; we immediately rejected sources which have only grating spectrometer observations due to severe pileup in the zeroth-order image (only the brightest sources have grating data). Most of the data sets use the nominal aim point on the ACIS-S3 chip, but we consider several ACIS-I archival observations.

We reprocessed the *Chandra* data sets to generate 0.3–10 keV level = 2 files using the *Chandra* Interactive Analysis of Observations (CIAO v4.0) data processing recipes ("threads")[8] with the most recent CALDB release (3.5.0). Times with noticeable background flares were excised by inspecting 0.3–10 keV light curves. A few comparison sample data sets contained the readout streak produced by bright sources, which we replaced, following the CIAO thread, with a strip of nearby background on either side of the central point source. The bright sources NGC 6251 and 3C 264 were observed in a 1/8-size subarray mode of the ACIS-S3 chip, but still produced a readout streak. Exposure-corrected final images were then produced from the energy-filtered level = 2 files following the standard CIAO thread, using the aspect solution file associated with each observation.

The core AGN X-ray emission was identified by matching the position of the X-ray source with the optical counterpart on the sky. More accurate positions were determined by binning the X-ray image and calculating the centroid.

2.3. Spectral Extraction

Our analysis (Section 3) is based on the properties and morphology of the ISM and IGM/ICM. Therefore, we reject galaxies from our preliminary sample where we do not detect strong extended thermal plasma. We determine the final sample in two steps: (1) we use radial profile fitting to reject sources with no extended emission and distinguish between multiple components of extended emission in the remainder. We extract spectra from regions corresponding to these extended components, then (2) reject sources whose extended emission is not fitted well by strong thermal components. We describe the first step presently and the second in Section 2.4.

[8] See http://cxc.harvard.edu/ciao/threads/index.html.

Extended emission on the chip may be made up of multiple sources. We use surface brightness profile fitting to distinguish between these sources, and based on these fits, define regions for spectral extraction to isolate each source as much as possible. We excised point sources from the level = 2 file, then extracted and fit radial profiles from annuli surrounding the AGN out to many kpc (scale depends on z). In many cases, no diffuse emission was detected above background. Where multiple components were found, we defined spectral extraction apertures based on the characteristic radii (r_0 from a β model) for each region. Compact emission centered on the AGN with r_0 smaller than the host galaxy we identified as "ISM," whereas very broad emission which declines slowly in surface brightness we identified with the "IGM/ICM." These are the labels used in Table 3; we note that the only sources included in Table 3 are those in which thermal emission has been verified. At the present stage, the purpose of these regions is solely to isolate different sources for spectral fitting.

For the larger, dimmer extended sources, the fits (and hence r_0) were less reliable. However, the slow decline of the "IGM" surface brightness means the spectra we extract are relatively insensitive to the size and shape of the region. Crucially, the spectral extraction apertures are *not* the same as those we use for our analysis in Section 3 and are defined only to isolate different sources. Spectra were extracted from these regions and were binned to at least 15 photons per bin to ensure the reliability of the χ^2 statistic; in high-quality spectra, the binning was as high as 100. In addition, we extract spectra for the unresolved AGN emission from detection cells using the 90% encircled energy radius as determined by the CIAO *mkpsf* tool. We return to the AGN spectra in Section 4.

2.4. Detection of Diffuse Gas

We fit models to the spectra we extracted (Section 2.3) to determine whether the emission is dominated by thermal plasma. Specifically, our sample consists of those galaxies in which the thermal emission surrounding the AGN appears dominant in number of photons, a point we return to below. We first ascertain the presence of hot gas by fitting the spectra extracted from each source using XSPEC v.12.5.0j (Arnaud 1996). In this paper, we exclusively use the `apec` model. This step is required since extended emission need not be thermal in origin—plausible nonthermal sources include power-law emission from the boundary shock of the cocoon inflated by the radio jets or from X-ray binaries (XRBs) in the host galaxy. Our fits all use a frozen Galactic $N_{\rm H}$ absorption component. After thermal emission is established, we then require the thermal component to be dominant at low energies. This ensures that the main contribution to the (energy-filtered) surface brightness is the thermal plasma. Of course, the hot atmospheres of many galaxies in our sample have been well studied (e.g., by *Chandra*; Table 1), but we wish to apply a uniform standard to all our sources including ones which have low signal.

For each spectrum, we first determine whether a single power-law or thermal model is a better baseline fit based on the χ^2 statistic, then add complexity as the degrees of freedom allow. In the case of thermal models, we begin by freezing the abundances with an isothermal model (there exists an abundance—normalization degeneracy in the absence of strong emission lines). Two-temperature (2-T) or multi-T models are invoked if an isothermal model is insufficient to fit the spectrum and the additional thermal component produces a better fit than a power-law component. It is worth asking whether a spectrum fitted well by a single thermal model is better fitted by a blend of power-law and thermal components. The answer is almost invariably "no." In very low signal spectra with few degrees of freedom, we conclude hot gas is present if a thermal model with reasonable parameters ($kT < 5.0$ and $0.1 < Z < 1.0$) is a better fit than a power-law model. We justify this assumption by the slopes of soft spectra: unabsorbed power-law emission tends not to fall off at the lowest energies, whereas thermal emission peaks near 1.0 keV. A "peaky" spectrum, even a low-signal one, is fitted better by a thermal model. As described in Section 2.3, we have attempted to isolate different sources, but we see the ISM and IGM in projection. We usually lack the signal for a deprojection analysis, so we first extract and fit a spectrum from the larger IGM region, then add the resultant models as frozen components in the ISM spectrum (keeping the normalization thawed). We find this produces better results than using a ring of IGM as background for the ISM spectra. It is possible that the power-law models are in fact describing thermal continua, but the thermal models which fit these spectra have inordinately high temperatures and often require suspiciously low abundances.

For a galaxy to be included in our final sample, we required the thermal component to be dominant between 0.3 keV $< kT <$ 2 keV. Due to *Chandra*'s energy-dependent effective area, even components with higher *luminosity* (e.g., an absorbed power law) may have many fewer photons in this range. This criterion allows us to characterize the morphology of only the hot plasma.

Up to this point we have treated our sources as uniformly as possible. Our analysis sample consists of the galaxies whose extended emission is dominated by thermal plasma, but we also reject sources with very complex morphology (3C 321, M84, M87, and 3C 305; Cyg A was retained after excising the inner cocoon). We remind the reader that we began with an XRG sample comprising those 13 galaxies within $z \sim 0.1$ with data in the *Chandra* archive. Of these, we have eight in our analysis sample. The preliminary comparison sample included 41 normal radio galaxies within the same cutoff, and of these we retain 18 (10 of which are FR II galaxies). Unfortunately, in many of the shorter XRG observations, we failed to detect significant diffuse emission. Notes on individual galaxies are in the Appendix, including those XRGs not included in our analysis sample (Appendix A.3). Sources we considered but rejected are listed in Table 2.

For those galaxies in our analysis sample, we provide the model fit parameters in Table 3. We also present the emission-weighted density $\bar{n}$ and average pressure $\bar{P} = \bar{n}kT_{\rm fit}$. $\bar{n}$ was computed by assuming the minor axis of the extraction region on the sky is the true minor axis and that the ellipsoid is axisymmetric in the minor axis (i.e., the axis along the line of sight is the minor axis). We report errors in Table 3 for one parameter of interest at $\Delta\chi^2 = 2.7$ (90%), but we do not report errors on $\bar{n}$ or $\bar{P}$ since there are unquantifiable sources of systematic error from our assumptions on the volume. The average densities and pressures are not particularly useful for studying any one system because profile information has been discarded; for most of our sources we cannot use deprojection. Our spectra with folded model fits are shown in Figures 3 (ISM), 4 (IGM), and 5 (AGN).

2.5. Radio and Optical Maps

We require high signal and high-resolution radio data in order to study the interaction between the radio lobes and the X-ray emitting gas. As the secondary lobes of XRGs are typically much fainter than the hot spots demarcating

Table 2
Rejected *Chandra* Observations

Name	z	Obs. IDs	Exp. Time (ks)	Obs. Type	Reason
		XRGs			
4C +32.25	0.052	9271	10	ACIS-S	a
4C +48.29	0.053	9327	10	ACIS-S	a
3C 136.1	0.064	9326	10	ACIS-S	a
J1101+1640	0.068	9273	10	ACIS-S	Mispointing
3C 223.1	0.107	9308	8	ACIS-S	a
		Archival normal radio galaxies			
M84	0.003	803 + 5908 + 6131	29 + 47 + 41	ACIS-S	b
M87	0.004	352 + 1808	38 + 14	ACIS-S	b
3C 84	0.018	333 + 428	27 + 25	HETGS	b+pileup
3C 442A	0.026	5635 + 6353 + 6359 + 6392	29 + 14 + 20 + 33	ACIS-I	b
3C 353	0.030	7886 + 8565	72 + 18	ACIS-S	c
3C 120	0.033	3015 + 5693	58 + 67	HETGS+ACIS-I	c
DA 240	0.036	10237	24	ACIS-I	a
3C 305	0.042	9330	8	ACIS-S	b
3C 390.3	0.056	830	34	ACIS-S	c
3C 382	0.058	4910 + 6151	55 + 65	HETGS	c+pileup
3C 33	0.059	6910 + 7200	20 + 20	ACIS-S	c
3C 35	0.067	10240	26	ACIS-I	a
0313−192	0.067	4874	19	ACIS-S	c
3C 105	0.089	9299	8	ACIS-S	a
3C 326	0.090	10242 + 10908	19 + 28	ACIS-I	Target not on chip
3C 321	0.096	3138	48	ACIS-S	b
3C 236	0.099	10246 + 10249	30 + 41	ACIS-I	c
3C 327	0.104	6841	40	ACIS-S	c
4C +74.26	0.104	4000 + 5195	38 + 32	HETGS	c
3C 184.1	0.118	9305	8	ACIS-S	a

Notes. Galaxies were selected for the preliminary sample as described in Section 2.1 and rejected for lack of diffuse gas or prohibitively complex morphology for our analysis (e.g., obvious multiple bubbles).
[a] No diffuse emission detected.
[b] Complex morphology.
[c] No diffuse thermal emission detected.

the terminal shocks of the active lobes, deep radio observations are often required to accurately determine their extent and angular offset from the active pair. The VLA is ideal for continuum band observations. Reduced VLA data for many of the sources are available through the NASA/IPAC Extragalactic Database (NED); references are provided in Table 1 where available. In some cases, we have reprocessed archival VLA data ourselves, and these are noted in Table 1.

In contrast to the requirement for high-quality radio data (needed to constrain the orientation of the radio jets and lobes), images from the (Palomar or UK Schmidt Telescope) Digitized Sky Survey (DSS) are usually sufficient for comparing the extent and alignment of the diffuse X-ray emitting gas to the distribution of optical light. Except in the case of B2 1040+31A, a close triple system, the optical emission on the relevant scales does not have significant contamination from companion sources. We note that the DSS spans our entire sample, whereas the higher resolution Sloan Digital Sky Survey (SDSS; Adelman-McCarthy et al. 2008) data are available for fewer than half of our sources. However, we compare the DSS images to the SDSS images where available, and note that good agreement is found in most cases for our model parameters (Section 3.2; Table 5). We also use published *Hubble Space Telescope* (*HST*) images, in particular those of Martel et al. (1999) for 3CR galaxies within $z < 0.1$. However, this survey is not sufficiently complete to replace the DSS data.

The images in Figures 1 and 2 show the data, using the higher quality SDSS images for the optical band where possible. Because of the differences in scale between radio galaxies and the different media which are important for lobe–gas interaction, the chip images we show are all processed slightly differently. In most cases, they have been smoothed with a Gaussian kernel of fixed σ (per galaxy) to enhance diffuse emission. Adaptive smoothing sometimes produces artificial structure in our images and is not used. Overlaid on the images of the ACIS chips are radio contours, and accompanying each X-ray image of the optical field on the same spatial scale. Figures 1 and 2 have been processed to represent the appearance of the sources and distribution of surface brightness on the sky, but we did not use these images directly in our analysis. In addition, the varying signal-to-noise ratios (S/Ns) in X-ray images do not necessarily correspond to real variation in source luminosity because the data sets come from observations of varying depth and redshift. Because some of the observations are shallow ($\leqslant$10 ks) or use the ACIS-I array, a non-detection of diffuse emission is not conclusive.

3. THERMAL ATMOSPHERE PROPERTIES

The models which assert that XRGs result from the interaction of the radio lobes with anisotropic gaseous environments (Capetti et al. 2002; Kraft et al. 2005) must ultimately be tested

Table 3
Thermal X-ray Spectral Parameters

Galaxy	Region	a (kpc)	b (kpc)	z	Gal. $N_{\rm H}$ (10^{20} cm^{-2})	kT (keV)	z	$\bar{n}$ (10^{-3} cm^{-3})	P (10^{-11} dyne cm^{-2})	Models	$L_{X,\rm th}$ (10^{41} erg s^{-1})	χ^2/d.o.f.
						XRGs						
B2 1040+31A	ISM	5	5	0.036	1.67	1.6 ± 0.4	0.3 (f)	38.	9.7	apec	1.6	4.66/5
...	IGM (s)	25	25	...	...	1.8 ± 0.2	1.0 (f)	3.8	1.1	apec	3.2	10.9/11
...	IGM (l)	75	75	...	...	$1.3^{+0.3}_{-0.1}$	$0.3^{+0.4}_{-0.2}$	1.1	0.24	apec	4.7	20.2/23
PKS 1422+26	IGM	85	40	0.037	1.54	0.89 ± 0.09	$0.3^{+0.2}_{-0.1}$	2.0	0.29	apec+PL	5.2	23.1/20
NGC 326	ISM	6	6	0.048	5.86	0.68 ± 0.05	1.0 (f)	28.	3.0	apec(+IGM)	5.4	13.3/17
...	IGM	166	94	...	...	3.6 ± 0.4	0.8 (f)	1.9	1.1	apec	10.	94.1/100
3C 403	ISM	9	6	0.059	12.2	0.24 ± 0.03	1.0 (f)	23.	0.89	apec+PL+$N_{\rm H}$(gauss+PL)	1.0	100.7/94
...	IGM	97	40	...	...	0.6 ± 0.2	1.0 (f)	0.37	0.04	apec	0.9	34.3/36
4C +00.58	ISM	17	17	0.059	7.14	1.2 ± 0.2	1.0 (f)	7.3	2.0	apec	3.0	5.8/6
3C 192	ISM+IGM	19	19	0.060	4.08	$1.0^{+2.2}_{-0.2}$	1.0 (f)	4.9	0.79	apec+$N_{\rm H}$(PL)	2.5	3.9/5
3C 433	ISM+IGM	44	26	0.102	7.77	0.96 ± 0.1	1.0 (f)	2.8	1.1	apec+PL+gauss	4.0	16.2/12
3C 315	IGM	200	110	0.108	4.28	$0.6^{+0.4}_{-0.1}$	1.0 (f)	1.0	0.1	apec+PL	8.2	4.5/10
						Comparison sample						
3C 449	ISM	5	5	0.017	8.99	0.77 ± 0.09	1.0 (f)	15.	1.9	apec(+IGM)	0.22	21.1/19
...	IGM	32	32	...	...	1.58 ± 0.06	0.8 ± 0.2	2.9	0.73	apec	3.9	179.8/169
3C 31	ISM	4	4	0.017	5.36	$0.68^{+0.04}_{-0.03}$	1.0 (f)	22.	2.4	apec(+IGM)	0.34	47.0/58
...	IGM	30	30	...	...	$2.0^{+0.5}_{-0.2}$	$0.4^{+0.2}_{-0.1}$	2.0	0.69	apec	1.3	143.1/138
3C 83.1B	ISM	3	3	0.018	13.4	0.65 ± 0.04	1.0 (f)	34.	3.6	apec(+IGM)	0.13	30.1/35
...	ICM	56	30	...	...	$8.^{+6}_{-3}$	1.0 (f)	1.2	1.6	apec	1.7	80.9/86
3C 264	ISM	5	5	0.021	1.83	0.34 ± 0.04	1.0 (f)	6.6	0.37	apec(+IGM)	0.18	19.7/30
3C 66B	ISM	9	9	0.022	7.67	$0.61^{+0.06}_{-0.04}$	$0.3^{+1.}_{-0.1}$	7.2	0.71	apec(+IGM)	0.36	49.8/42
3C 296	ISM	9	7	0.024	1.92	0.76 ± 0.02	1.0 (f)	9.0	1.1	apec(+IGM)	1.3	49.0/46
...	IGM	75	75	...	...	$4.^{+4}_{-1}$	1.0 (f)	0.8	0.5	apec	0.8	18.2/19
NGC 6251	ISM	6	6	0.024	5.59	0.66 ± 0.03	1.0 (f)	14.	1.5	apec(+IGM)	1.0	110./111
PKS 2153−69	ISM	7	7	0.028	5.59	0.77 ± 0.07	1.0 (f)	10.	1.2	apec(+hot IGM)	1.4	26.0/24
...	IGM	32	32	...	...	$T_1 = 3.0^{+2.}_{-1.}$	1.0 (f)	2.6	1.3	apec+apec	6.8	41.8/42
...	...	...	...	...	...	$T_2 = 0.9 \pm 0.06$	1.0 (f)					
3C 338	ICM	30	30	0.030	0.89	$T_1 = 1.8^{+0.2}_{-0.1}$	0.7 ± 0.05	28.	17.	apec+apec	434.	432.5/390
...	...	...	...	...	...	$T_2 = 5.0^{+1.}_{-0.5}$	0.7 ± 0.05					
3C 98	IGM	46	31	0.030	10.8	$1.1^{+0.3}_{-0.2}$	$0.2^{+0.4}_{-0.1}$	1.8	0.32	apec	0.8	8.5/11
3C 465	ISM	6	6	0.031	4.82	1.12 ± 0.08	1.0 (f)	20.	3.6	apec(+IGM)	1.4	30.4/32
...	IGM	80	56	...	...	$4.2^{+0.5}_{-0.3}$	1.0 (f)	2.3	1.6	apec+gauss	25.	176.8/164
3C 293	ISM	8	5	0.045	1.27	1.0 ± 0.3	0.2 (f)	28.	4.4	apec(+IGM)	1.6	0.7/4
Cyg A	ICM	140	140	0.056	30.2	$T_{\rm low} = 3.2^{+1.3}_{-0.1}$	0.6 (f)	4.8	6.0	cflow	1600	433.1/403
...	...	...	...	...	...	$T_{\rm high} = 18. \pm 7.$						
3C 445	IGM	73	54	0.056	4.51	$0.7^{+0.3}_{-0.4}$	1.0 (f)	0.26	0.03	apec+PL	0.6	9.38/14
3C 285[a]	ISM+IGM	30	30	0.079	1.27	$T_1 = 1.2^{+0.4}_{-0.2}$	1.0 (f)	2.3	0.13	apec+apec	2.9	6.9/7
...	...	...	...	...	...	$T_2 = 0.33^{+0.3}_{-0.05}$	1.0 (f)					
3C 452	IGM	201	82	0.081	9.64	3.8 ± 0.1	1.0 (f)	1.3	0.79	apec+PL	5.0	148.7/155.
3C 227	ISM+IGM	28	28	0.087	2.11	$T_1 = 0.2$ (f)	1.0 (f)	5.9	1.0	apec+apec+gauss	7.4	12.7/29
...	...	...	...	...	...	$T_2 = 1.2^{+0.3}_{-0.2}$	1.0 (f)					
3C 388	ICM(bar)	16	16	0.091	5.58	2.4 ± 0.2	1.0 (f)	24.	9.2	apec	41.	38.9/40
...	ICM(big)	130	130	...	...	3.3 ± 0.1	1.0 (f)	3.1	1.7	apec	425.	174.9/200

Notes. Diffuse atmosphere spectral parameters for targets in Table 1. (f) denotes a frozen parameter. In calculating $\bar{n}$, we assume axisymmetry and use a volume $V = ab^2$. Unabsorbed luminosities are reported for the thermal component only; in the case of the ISM, this is the cooler component. The notation (+IGM) indicates that a thermal model with all parameters except the normalization frozen was used in the fit; these parameters are based on fits to the IGM.
[a] 3C 285 is difficult to disentangle, but the larger IGM values agree with those coincident with the ISM.

by direct observations of these environments. In particular, we wish to know whether the correlation described in C02 exists in the X-ray band, i.e., whether XRGs are preferentially found in systems where the jets are directed along the major axis of the gas distribution.

This objective can be distilled into two distinct questions. First, the observed correlation between the XRG secondary lobes and the minor axis of the host galaxy was taken by C02 to imply that the minor axis of the ISM in these galaxies was similarly aligned. But how well does the X-ray gas trace

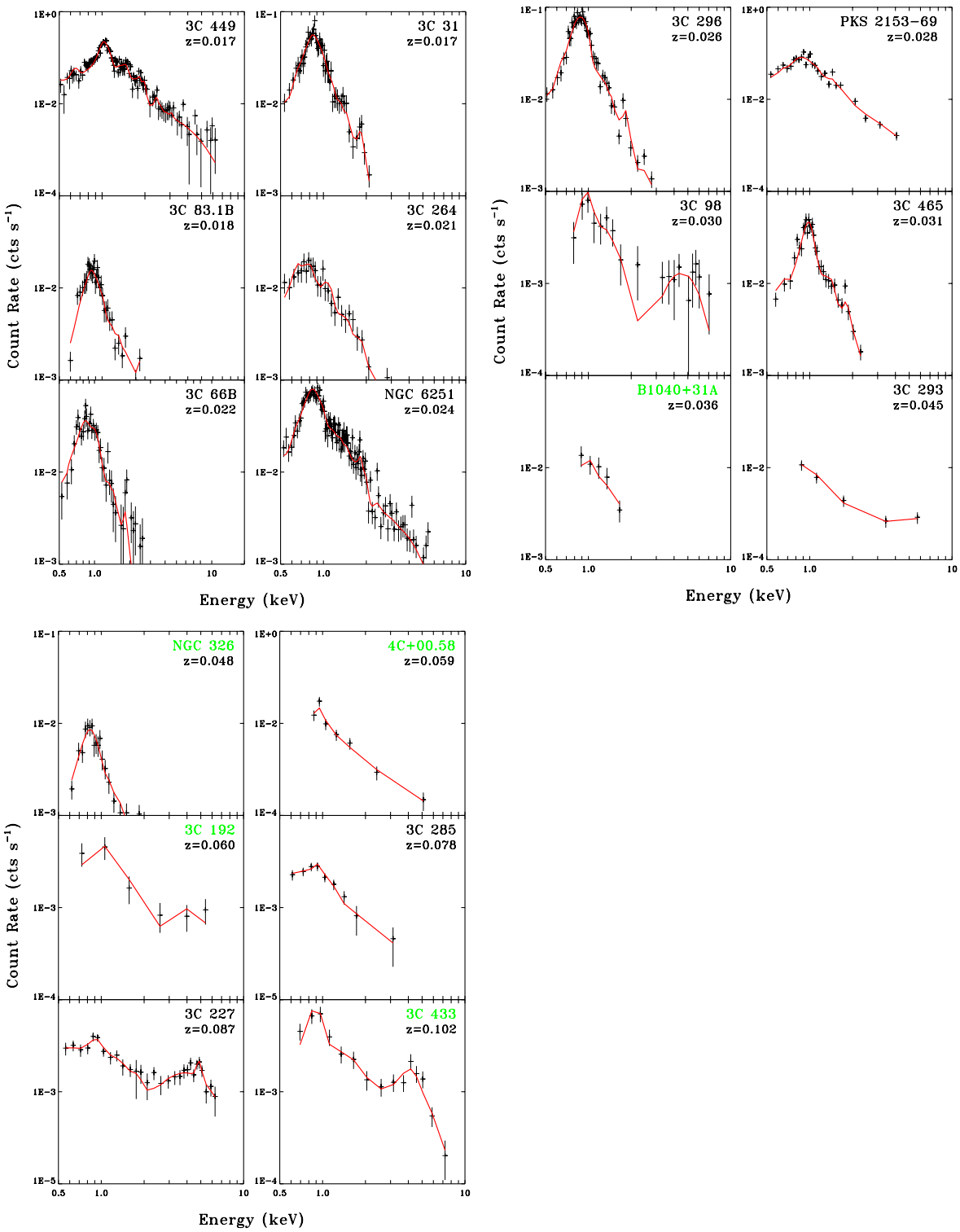

Figure 3. Spectra of the X-ray ISM we use in our morphology comparison (Table 5). The XRG sample is shown with galaxy names in green and the total model fit has been plotted over the data in red. The values can be found in Table 3. Note that 3C 403 is shown in Figure 5 since the ISM is small compared to the PSF and is isolated via energy filtering (Kraft et al. 2005).

(A color version of this figure is available in the online journal.)

the optical isophotes? Second, is there a systematic difference between the orientation of the radio lobes and the X-ray gas distribution in XRGs and normal radio galaxies? In other words, does the C02 correlation exist in the media which interact with the radio lobes? These questions are distinct in part because the medium responsible for shaping the XRGs in the backflow models is not necessarily the ISM, but may be the IGM/ICM. Because these questions rely on our measurement of gas morphology, we first describe our image fitting method, which consists of fitting ellipses to measure ellipticity ($\epsilon \equiv 1 - b/a$) and position angle (P.A.) of the X-ray emission on the sky.

Table 4
Optical Hosts Comparison

Name	ϵ_{DSS}			P.A.$_{DSS}$			P.A.$_{radio}$		
	This Work	C02	S09	This Work	C02	S09	This Work	C02	S09
Working Sample									
B2 1040+31A	0.15	...	...	153	...	...	159	...	...
PKS 1422+26	0.16	...	...	118	...	...	92	...	...
NGC 326	0.04	...	0	153	...	b	120	...	135
3C 403	0.27	a	0.25	39	35	39	72	85	79
4C +00.58	0.51	...	...	139	...	...	65	...	...
3C 192	0.02	a	0	119	95	b	123	125	123
3C 433	0.30	...	0.47	167	...	145	169	...	164
3C 315	0.37	a	0.46	44	35	33	12	10	8
Unused XRGs									
4C +32.25	0.12	a	0.15	90	90	84	61	60	64
4C +48.29	0.03	...	0	127	...	b	179	...	170
3C 136.1	0.39	a	0.37	101	100	117	106	110	139
J1101+1640	0.34	...	0.29	62	...	64	113	...	114
3C 223.1	0.42	a	0.45	43	40	40	7	15	15

Notes. A " ... " signifies no data exist in the literature for comparison. Note that while radio position angles are generally in agreement, large discrepancies exist (attributable to where the jet/lobe P.A. is measured). Uncertainties are not quoted in C02 or S09.

[a] Capetti et al. (2002) do not provide ϵ values in their paper.

[b] Saripalli & Subrahmanyan (2009) do not report an optical P.A. if ϵ is "0."

3.1. Ellipse Fitting

We determine the gross morphology of the hot gas by fitting ellipses to the X-ray emission and finding the characteristic ϵ and P.A.—gross elongation and orientation—of the surface brightness. We treat the surface brightness as a two-dimensional "mass" distribution and compute the moment of inertia tensor within an aperture chosen by the scale of the medium (a point we return to below). From this, we measure the principal axes corresponding to the characteristic major and minor axes of the distribution. Of course, the gas distribution may well have complexity beyond that captured by a simple elliptical model—however, most of our data do not justify higher-order models. We describe our method presently.

Our generic ellipse-fitting routine takes as input a processed surface brightness distribution on the chip (see below). To determine the principal axes, we use the QL method with implicit shifts (Press et al. 1992) to find the eigenvalues of the tensor, whereas the P.A. is determined by the orientation of one of the eigenvectors. We use the IDL `eigenql` function[9] realization of this method. The QL method with implicit shifts is a method for finding the eigenvalues of a matrix by decomposing it into a rotation matrix "Q" and a lower triangular matrix "L;" by virtue of the decomposition, the eigenvalues of the original matrix appear on the diagonal of the lower triangular matrix at the end. To determine the 2σ error bars reported in Table 5, we use the bootstrap resampling method over 10^4 iterations (Efron 1982). We adopt this method since it is better suited to low count rate images than the standard *Sherpa*[10] two-dimensional fitting routines.

Our treatment of the surface brightness prior to the fitting described above differs slightly between the bright and compact ISM and the faint, extended IGM/ICM. Within each regime, we attempt to treat each data set uniformly; any additional processing is noted in the Appendix.

1. *Interstellar medium.* For the ISM, we use no additional binning beyond the *Chandra* resolution (and thus cannot subtract a constant background). This choice is motivated by the desire to minimize artificial smoothing due to the relatively small scales of the ISM. However, we do apply the exposure correction across the medium as an adjustment to the brightness of each pixel, and we energy filter the image based on the spectrum. The radius of the (circular) aperture we use is straightforwardly determined from a one-dimensional radial profile extracted from annuli centered on the AGN. We excise the AGN emission through energy filtering and masking a point-spread function (PSF) we created at the location of the AGN using the CIAO tool *mkpsf*. We mask the region corresponding to the 95% encircled energy ellipse. One might worry that (especially with very bright AGN) this procedure would bias our measured ϵ or P.A., but this appears not to be the case; the AGN is also usually centered on the nominal aim point, so ϵ_{PSF} is usually small. The remaining counts within the aperture are fed into our ellipse-fitting routine. Because background is not subtracted, the bootstrap method is likely more accurate, but our measured ϵ values are systematically low (though not *very* low thanks to the high contrast of the compact ISM). We note that toggling pixel randomization appears to have no effect on our results.
2. *Intragroup/intracluster medium.* Because the IGM is typically quite faint and extended, we must bin the chip quite coarsely to see the enhanced surface brightness. We mask the ISM and all other point sources, then bin to 16×16 pixels and apply a similarly binned exposure correction. Energy filtering is applied based on the spectrum. Finally, we smooth the image with a Gaussian kernel ($\sigma = 2$ coarsely binned pixels). We subtract background levels using either empty regions on the chip (if the visible extent of the IGM is small) or blank sky files if the medium fills the chip. The background files are similarly energy filtered and binned/smoothed. We choose circular apertures motivated by the idea that all our radio galaxies have escaped the ISM, but only some have escaped the "local" IGM (Section 3.3). By "local" IGM, we specifically mean we use an aperture guided by the characteristic radius r_0 determined in one-dimensional radial profile fitting centered on the radio galaxy. Where r_0 is not well constrained, we take an aperture roughly bounding the "2σ" isophote (where "1σ" is taken to be the background level in the binned, smoothed image). We then fit the IGM assuming it is a smooth ellipsoid on the scales of interest (i.e., no internal structure) so the range in plate scale is not important between galaxies. A brief inspection of the isophotes indicates that this is a good first-order description on large scales, but wrong near the center. Inside our chosen aperture, the bootstrap method essentially tracks the contrast of structure against noise, so the uncertainty is also a function of the background level we subtract. Nonetheless, the P.A.s are reasonably constrained. Notably, there are a few cases where there is strong IGM/ICM not centered on the galaxy (NGC 326 and 3C 83.1B), but we ignore the emission that cannot be "seen" by the radio galaxy. Additionally, in B2 1040+31A, the most significant IGM is a smaller structure centered on the radio galaxy's host system enveloped in a larger, much dimmer

[9] Source code available from http://imac-252a.stanford.edu/programs/IDL/lib/eigenql.pro.

[10] See http://cxc.harvard.edu/sherpa.

Table 5
Ellipse Parameters for the ISM

Name	ϵ_{X-ray}	P.A.$_{X-ray}$ (°)	$\epsilon_{X-ray\ PSF}$	P.A.$_{X-ray\ PSF}$ (°)	ϵ_{DSS}	P.A.$_{DSS}$ (°)	ϵ_{SDSS}	P.A.$_{SDSS}$ (°)	P.A.$_{jets}$ (°)	P.A.$_{wings}$ (°)
XRGs										
B2 1040+31A	0.21 ± 0.07	158 ± 11	0.07	58	...	...	0.15 ± 0.02	153 ± 22	159	58
NGC 326	0.084 ± 0.009	130 ± 37	0.09	134	0.037 ± 0.004	153 ± 33	...	...	120	42
3C 403	0.47 ± 0.03	35 ± 5	0.11	108	0.27 ± 0.09	39 ± 35	...	...	72	133
4C +00.58	0.15 ± 0.02	138 ± 17	0.07	161	0.51 ± 0.08	139 ± 6	0.44 ± 0.02	138 ± 3	65	14
3C 192	0.04 ± 0.01	126 ± 22	0.06	146	0.018 ± 0.005	119 ± 40	0.018 ± 0.002	132 ± 38	123	54
3C 433	0.09 ± 0.02	156 ± 40	0.04	172	0.3 ± 0.1	172 ± 21	...	...	169	84
Comparison sample										
3C 449	0.14 ± 0.02	6 ± 15	0.16	30	0.21 ± 0.03	8 ± 6	...	...	9	
3C 31	0.087 ± 0.003	112 ± 16	0.18	159	0.10 ± 0.01	142 ± 12	...	...	160	
3C 83.1B	0.17 ± 0.01	166 ± 16	0.12	1	0.19 ± 0.02	161 ± 17	...	...	96	
3C 264	0.042 ± 0.002	129 ± 27	0.17	148	0.044 ± 0.003	129 ± 27	0.011 ± 0.005	160 ± 32	30	
3C 66B	0.15 ± 0.01	128 ± 9	0.15	13	0.13 ± 0.01	131 ± 15	...	...	60	
3C 296	0.15 ± 0.02	137 ± 6	0.17	147	0.19 ± 0.02	151 ± 13	0.23 ± 0.01	147 ± 6	35	
PKS 2153−69	0.22 ± 0.03	106 ± 8	0.17	34	0.25 ± 0.04	126 ± 12	...	...	136	
NGC 6251	0.047 ± 0.002	25 ± 23	0.15	72	0.11 ± 0.01	24 ± 13	...	...	115	
3C 98	0.19 ± 0.04	92 ± 24	0.13	90	0.10 ± 0.03	62 ± 20	...	...	10	
3C 465	0.061 ± 0.003	51 ± 29	0.17	74	0.17 ± 0.08	33 ± 25	...	...	126	
3C 293	0.30 ± 0.07	84 ± 18	0.05	110	0.50 ± 0.06	64 ± 7	0.29 ± 0.05	60 ± 10	126	
3C 285	0.21 ± 0.03	141 ± 18	0.19	96	0.36 ± 0.06	133 ± 13	0.36 ± 0.05	125 ± 9	73	
3C 227	0.11 ± 0.01	19 ± 20	0.33	98	0.09 ± 0.02	27 ± 17	...	...	65	

Notes. Position angles (P.A.s) are reported counterclockwise from north (0°) and chosen to reflect the acute angle between the major axes of the X-ray, optical, and radio ellipses. The error bars are reported at 95% using our ellipse-fitting method (Section 3.1). Radio P.A.s are estimated visually and have an estimated error of ΔP.A. ∼ 10°. The PSF values are reported for the best-fit PSF used to mask the AGN emission.

atmosphere with a different P.A. Using the methods above, we take the smaller structure to be the local IGM.

We treat the optical DSS data similarly. We do not further bin the images and we measure the background near the host galaxy (but away from companions, which we mask). We use an aperture corresponding to the extent of the hot ISM emission. We wish to use similar apertures in the X-ray and optical images because ϵ may (physically) vary with r. In the inner optical isophotes, both ϵ and P.A. may be (artificially) radially dependent due to convolution with the PSF and viewing a triaxial object (isophotal "twists"), respectively, (Binney & Merrifield 1998). Inner isophotes have dramatically lower values of ϵ than the outer "real" values (as in Tremblay et al. 2007). The isophotal twists, on the other hand, are a consequence of viewing a triaxial object at a viewing angle not aligned with any of its axes. Either is potentially a problem for our optical fitting when the X-ray ISM aperture is small, but usually the X-ray emission is extended sufficiently that most of the optical light in our aperture comes from regions where $d\epsilon/dR$ is small; isophotal twists are only seen in the very central regions of a few nearby galaxies in our DSS data. None of our sources are quasars or appear to be saturated.

3.2. Optical–X-ray Correlation

Because long (50–100 ks) exposures are often required to see the diffuse X-ray gas even in nearby galaxies, it is plainly attractive to adopt the optical light as a proxy for the hot ISM. To zeroth order the stars and ISM should coincide, but the ISM may not be in hydrostatic equilibrium with the host (Diehl & Statler 2007), and may be disturbed by recent mergers presumed to power the AGN. In fact, Diehl & Statler (2007) find (in an analysis of 54 *Chandra* detections of hot ISM) that the gas ellipticity and morphology differ significantly from the starlight,

Table 6
Ellipse Parameters for the Local IGM/ICM

Name	ϵ_{IGM}	P.A.$_{IGM}$ (°)	P.A.$_{jets}$ (°)	P.A.$_{wings}$ (°)
XRGs				
B2 1040+31A	0.18 ± 0.08	130 ± 30	159	58
PKS 1422+26	0.13 ± 0.03	88 ± 14	92	179
NGC 326	0.20 ± 0.04	128 ± 20	120	42
4C +00.58[a]	0.15 ± 0.02	138 ± 17	65	14
3C 315	0.38 ± 0.06	23 ± 7	12	120
Comparison sample				
3C 449	0.3 ± 0.1	41 ± 12	9	...
3C 31	0.18 ± 0.01	123 ± 4	160	...
3C 296	0.23 ± 0.04	121 ± 8	35	...
PKS 2153−69	0.13 ± 0.03	140 ± 10	136	...
3C 338	0.243 ± 0.002	65 ± 6	90	...
3C 465	0.37 ± 0.02	53 ± 3	126	...
Cyg A	0.2 ± 0.1	22 ± 4	115	...
3C 445	0.3 ± 0.1	77 ± 8	169	...
3C 285	0.28 ± 0.06	163 ± 9	73	...
3C 452	0.43 ± 0.03	83 ± 2	78	...
3C 388 (l)	0.13 ± 0.02	65 ± 6	55	...
3C 388 (s)	0.088 ± 0.005	133 ± 18	55	...

Notes. The error bars are reported at 95% using our ellipse-fitting method but are likely underestimates. Images are processed before fits (Section 3.1) by binning and smoothing due to the extended faint emission. For 3C 388 we use the large (l) ICM value, but note the smaller ICM has a distinct position angle (Section 3.3).

[a] The same values for 4C +00.58 are used in the ISM ellipse table. The identity of the medium we fit is ambiguous.

although their sample only overlaps our own by a small amount. Acknowledging that a detailed view of the inner ISM shows

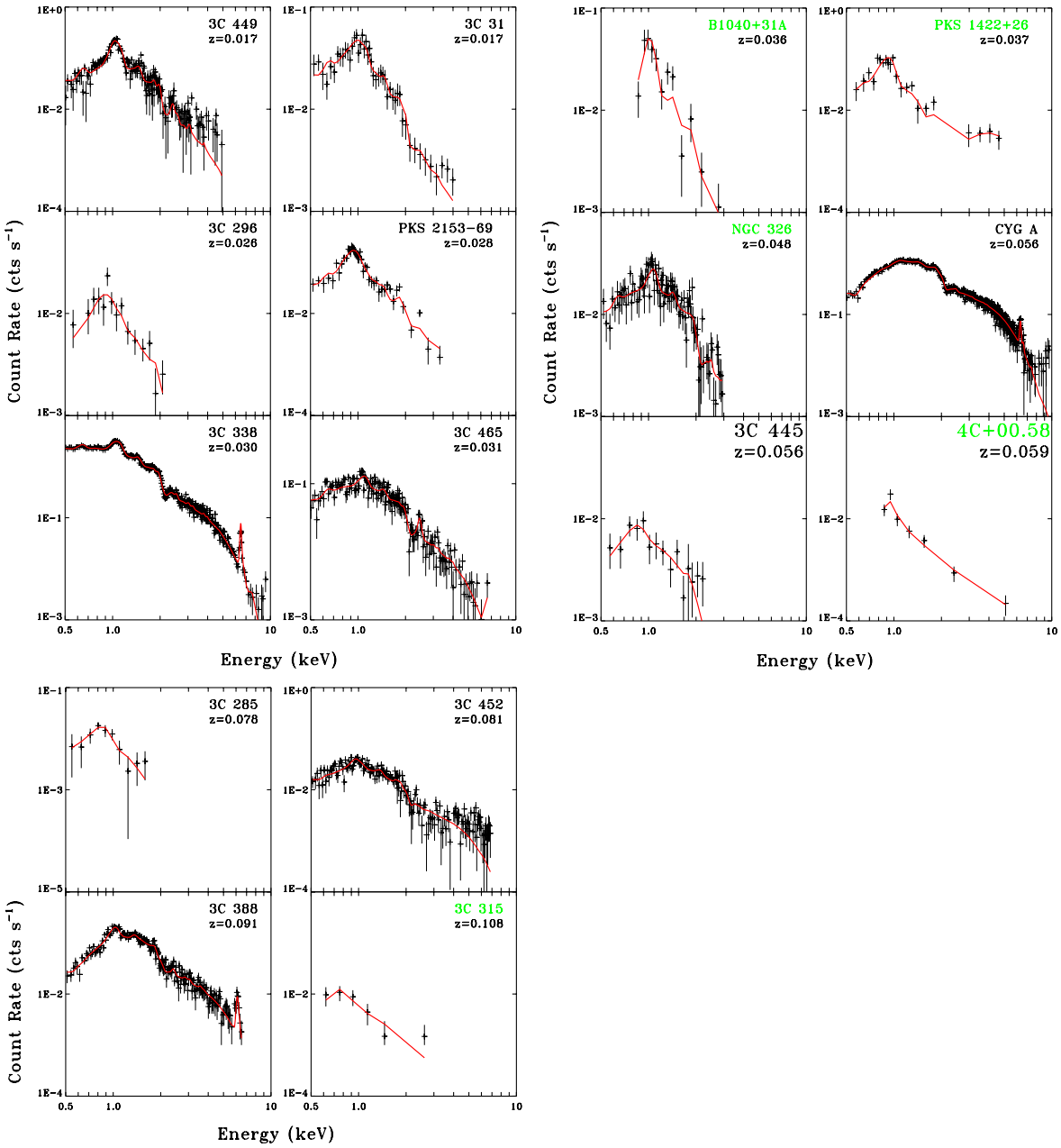

Figure 4. Spectra of the X-ray IGM we use in our morphology comparison (Table 6). The XRG sample is shown with galaxy names in green and the total model fit has been plotted over the data in red. The values can be found in Table 3.

(A color version of this figure is available in the online journal.)

significant differences from the starlight, we ask whether the starlight is a sufficient proxy for the ISM in gross morphology (i.e., we are interested in the outer X-ray "isophotes") or whether it is of such different character that it weakens the Capetti et al. (2002) and Saripalli & Subrahmanyan (2009) analyses.

In fact, our work supports the identification of the optical light as an appropriate proxy for the hot ISM. However, in contrast to C02, we do not find that XRGs are preferentially in galaxies with higher ϵ, although we note that our X-ray ϵ values are probably underestimated. For the subset of our combined sample with strong ISM emission (19 of 26 galaxies), we find a correlation coefficient of $R = 0.60$ (Figure 6) between the ellipticity of the X-ray light ($\epsilon_{\text{X-ray}}$) and the ellipticity of the host galaxy in the DSS images (ϵ_{DSS}). The correlation between the P.A.s of the best-fit ellipses is even stronger ($R = 0.96$), but this is not meaningful because we expect a positive correlation even if the ellipses are misaligned. This is because an ellipse may have a P.A. anywhere between $0^\circ <$ P.A. $< 180^\circ$, but when considering the angular separation of the P.A.s of two superimposed ellipses, one of the angles of separation must be acute. Therefore, a better measurement of the agreement between the optical and X-ray P.A.s is shown in Figure 6 where the distribution of ΔP.A. $=$ P.A.$_{\text{ISM}} -$ P.A.$_{\text{optical}}$ is shown. The values in Figure 6 are presented in Table 5. The uncertainties are given at the 2σ level from the bootstrap method. For $N = 21$, our results are significant at the 95% level. The values we use are given in Table 5 along with a comparison of DSS to SDSS values (and our ISM values to the best-fit AGN PSF values).

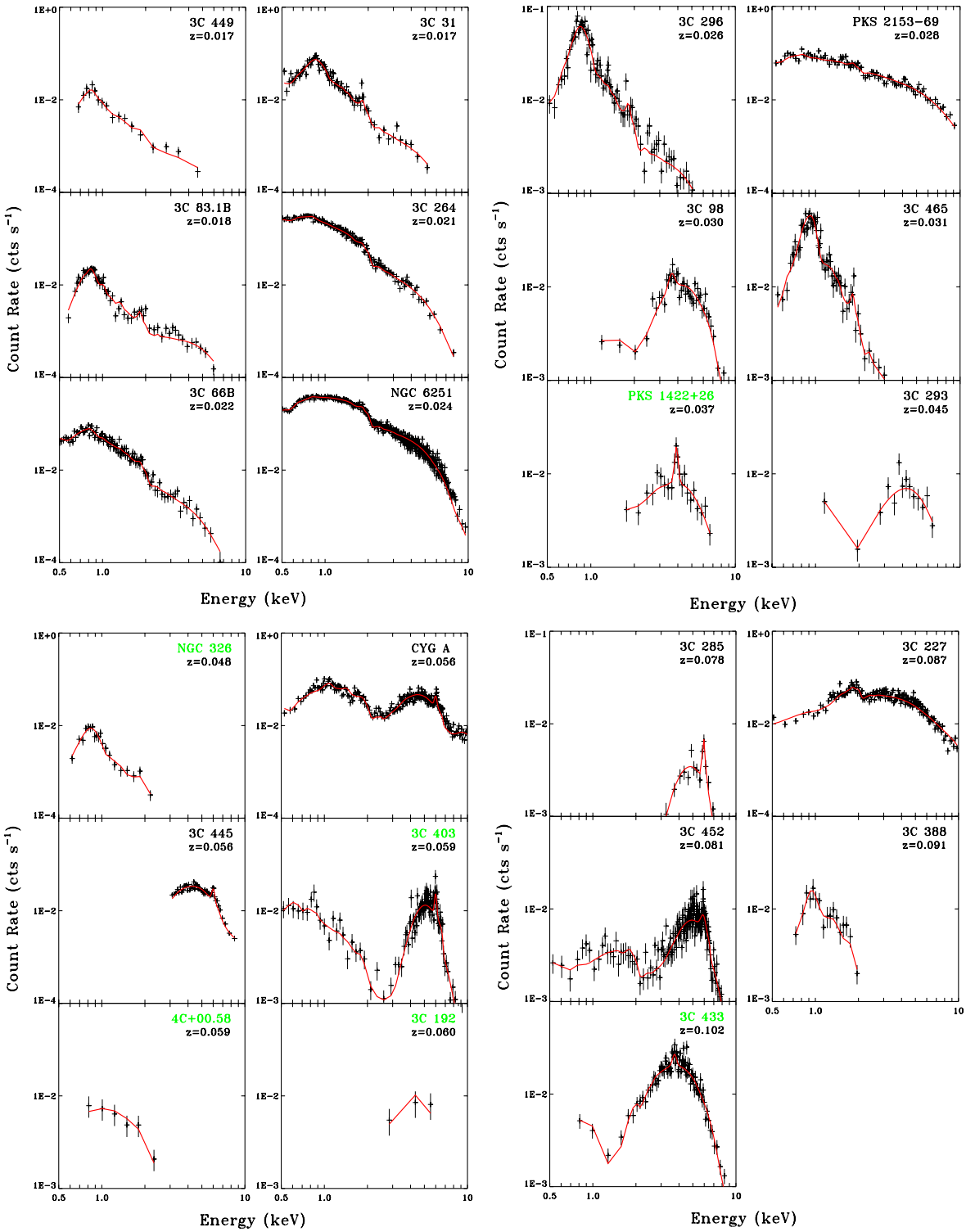

Figure 5. Spectra extracted from the central PSF of the host galaxy; emission may come from either the parsec-scale jet or accretion disk region. The total model fit has been plotted over the data in red and XRG galaxies have their names in green. The spectra are essentially broken into absorbed and unabsorbed spectra; some of the unabsorbed spectra require thermal components. Note that 3C 338 has no detected AGN emission and 3C 403 has a small ISM represented in the spectrum of the area near the AGN.

(A color version of this figure is available in the online journal.)

We check our results for the optical values against the literature, where profile and isophotal fitting is standard. Our distribution of optical ϵ peaks slightly below $\epsilon = 0.2$ and falls off quickly at higher values. This is in agreement with the *HST* study by Martel et al. (1999), but is slightly rounder than the reported distributions in the ground-based studies of radio galaxies by Smith & Heckman (1989) and Lambas et al. (1992), whose distributions peak at $\epsilon = 0.2$ and 0.25, respectively. The small excess of very round hosts may be real (it persists even when ϵ is measured at larger radii than reported) but our

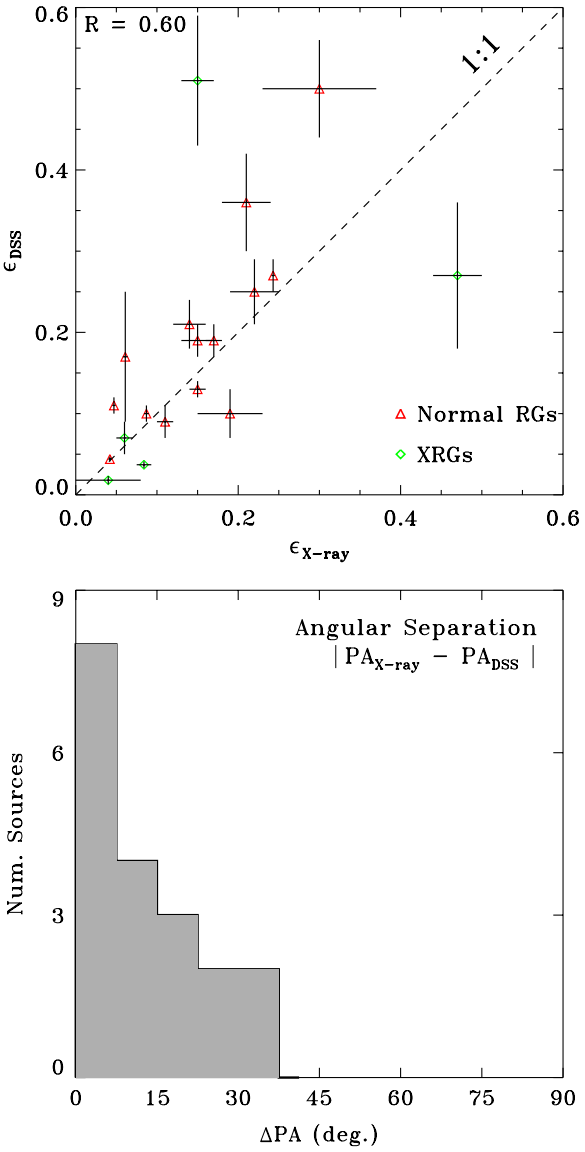

Figure 6. Top: Comparison of the eccentricities of the diffuse ISM to the optical light where ϵ in each case has been generated by our ellipse-fitting method (Section 3.1). The dashed line represents a 1:1 correlation rather than a best-fit line. Bottom: Comparison of the P.A.s of the best-fit ellipses for the diffuse ISM to those of the optical light where the values are determined by our ellipse-fitting method (Section 3.1).

(A color version of this figure is available in the online journal.)

method may also underestimate ϵ. The ϵ measurement has been made for far fewer sources in the X-ray band so a systematic comparison is difficult. In addition, we compare our optical ϵ and P.A. values for the XRG sample specifically to any matching sources in the C02 and S09 studies (Table 4) and find generally good agreement. In other words, in the X-ray band we (to some extent) reproduce the C02 and S09 results.

Additionally, we note here a few caveats. First, we do not take into account the possible XRB contamination of the ISM. We do not consider this a significant problem based on our spectroscopic analysis—even though low-mass X-ray binary (LMXB) spectra are often stronger at lower energies, the thermal models are much better able to fit the peaks in the ISM spectra, and are often sufficient for an adequate fit without requiring a power law. This is consistent with Sun et al. (2005) who demonstrate that the XRB contribution to the emission is usually less than 10% of the luminosity; in many of our spectra we lack the signal to distinguish a $< 10\%$ contribution. Second, as noted in Section 3.1, our X-ray ϵ values tend to be systematically underestimated. This makes a comparison with, for example, the Diehl & Statler (2007) work difficult. Notably there is one strong outlier in 3C 403, whose $\epsilon_{\text{X-ray}} = 0.47 \pm 0.03$ is much higher than its optical ellipticity. Kraft et al. (2005) find an even higher value of $\epsilon_{\text{X-ray}} = 0.57 \pm 0.04$ using a profile fitting technique (they also compare $\epsilon_{\text{X-ray}}$ to *HST* $\epsilon_{\text{optical}}$), so it appears likely that the 3C 403 ISM is indeed out of equilibrium. However, the case of 3C 403 is noteworthy in that the small extent of the ISM relative to the AGN emission makes energy filtering a more effective way to remove the AGN prior to fitting. Kraft et al. (2005) use a 0.3–1.0 keV window, but it is difficult to conclude with certainty that this emission is "dominated" by the hot gas because it is possible to obtain a good fit to the spectrum (shown in Figure 5) using an unabsorbed power law between 0.3 and 2.0 keV. If 3C 403 is indeed badly out of equilibrium, it appears to be an isolated case in our sample.

3.3. X-ray–Radio Correlation

We now measure the correlation between the P.A.s of the X-ray media and the radio jets by asking whether the quantity $\Delta\text{P.A.} = |\text{P.A.}_{\text{radio}} - \text{P.A.}_{\text{X-ray}}|$ is uniformly distributed for the XRGs and normal radio galaxies. A uniform distribution means that for a given sample there is no preferred alignment between the radio jets and the P.A. of the surrounding hot gas. The radio jets are highly collimated and their orientation is determined "by eye;" we believe the values are accurate to within 10°. The ellipticity and P.A. of the X-ray emission are determined as described in Section 3.1, but to which medium shall we compare the alignment of the jets? Our goal is to determine whether XRGs reside preferentially in media elongated along the jet axis. In the overpressured cocoon model, this medium is assumed to be the ISM, but there are a few XRGs (NGC 326 and PKS 1422+26) for which the ISM cannot be the "confining" medium because the wings are produced outside the ISM. Therefore, we must consider how to deal with the IGM/ICM. We describe the process of IGM/ICM aperture selection after our ISM comparison. In our discussion, the "relevant" medium is the one which could potentially confine the radio galaxy.

1. *Interstellar medium.* All of our radio galaxies have escaped the ISM, but it must have been the relevant medium for all of them at early stages. Assuming that the jet orientation relative to the ISM has not changed over the life of the radio galaxy, it is straightforward to compare ΔP.A. for the normal radio galaxies and the XRGs using the ISM. In the C02 model, we expect that the XRGs would have a small angular separation between the ISM major axis and the radio jets, i.e., $\Delta\text{P.A.} \sim 0$. Figure 7 bears this expectation out (values reported in Table 5). The aperture for the ISM was the same as described in Section 3.2 and we exclude the same five galaxies. Figure 7 includes six XRGs and shows the distributions of both the active and secondary lobes. As noted in Section 3.2, the agreement between the gas and the starlight is good. Neither XRG distribution is consistent with a uniform distribution ($P = 0.04$ for the primary lobes and 0.01 for the secondary lobes) despite the small sample size, whereas the normal radio galaxies are consistent with uniform distributions ($P \sim 10\%$). The normal FR I ΔP.A. distribution is only marginally consistent with uniform (although dramatically different from the XRGs) and may

be influenced by the giant radio galaxies which S09 noted tend to have jets aligned along the *minor* axis of the host. This result is, in our view, strong evidence for the C02 model, although it was anticipated from Section 3.2. The IGM may be the confining medium for several XRGs, but the strong agreement with the C02 geometry in the ISM suggests that the ISM–jet orientation may be intrinsically important. The overpressured cocoon model put forth to explain this geometry should not be confused with the observed result.

2. *Intragroup/intracluster medium.* Because the XRGs exist whose wings could not have been produced by the ISM in the C02 model, we want to see if the C02 geometry exists among IGM atmospheres as well. We thus have to consider how to choose apertures in the IGM/ICM for the comparison sample as well. There is no obvious way to compare these media for various radio galaxies, especially since some of our control sample radio sources extend far beyond the chip boundaries.

   However, using the same logic as above, we can measure the elongation and orientation of the "local" IGM/ICM (Section 3.1). All sources larger than the local IGM/ICM must have passed through it at one point, and it is the relevant medium for all sources enclosed by it and outside the ISM. As mentioned in Section 3.1, we assume that the IGM/ICM is described by a smooth ellipsoid so the P.A.s are comparable between sources of vastly different scale (the gradients are more important). We therefore expect the ΔP.A. values to be uniformly distributed in the control sample.

   We detect IGM/ICM emission in fewer galaxies, but we include the five galaxies with IGM/ICM but no clearly distinguishable ISM (3C 338, 3C 388, 3C 445, 3C 452, and Cyg A). We thus have five normal FR I galaxies, seven normal FR II galaxies, and five XRGs. Of the XRGs, the IGM/ICM is the relevant medium for NGC 326 and PKS 1422+26, and may be the relevant medium in 3C 315, 4C +00.58, and B2 1040+31A. Although the sample sizes are smaller, the ΔP.A. distributions for the FR I and II galaxies are consistent with uniform ($P = 0.3$ and 0.4, respectively; Figure 8). The XRG sample, on the other hand, is not consistent with a uniform distribution ($P = 0.02$ for both the primary and secondary lobes). Our values are found in Table 6.

   In 3C 452, the X-ray emission traces the radio emission so well that the geometry of the extended emission probably represents the radio galaxy cocoon or a bounding shock and not the actual IGM (even when a purely "thermal" image is reconstructed; Appendix A.1). Similarly, the radio lobes of 3C 388 may be responsible for the geometry of the surrounding medium and the inner isophotes of the surrounding ICM are elongated perpendicular to the jet. If we exclude 3C 452 and use a smaller aperture in 3C 388 as the "local" ICM, our results for the IGM/ICM comparison outlined above are unchanged (the normal FR II galaxies still look uniformly distributed).

We cannot easily compare a mix of ISM and IGM/ICM relevant media in the XRG sample to the comparison sample. However, we can do this for the XRG sample because we have the additional spatial information of the secondary lobes. When we use the IGM values for NGC 326 and PKS 1422+26, the distribution of ΔP.A. obeys the C02 correlation even more strongly than for the ISM or IGM alone. The probability that

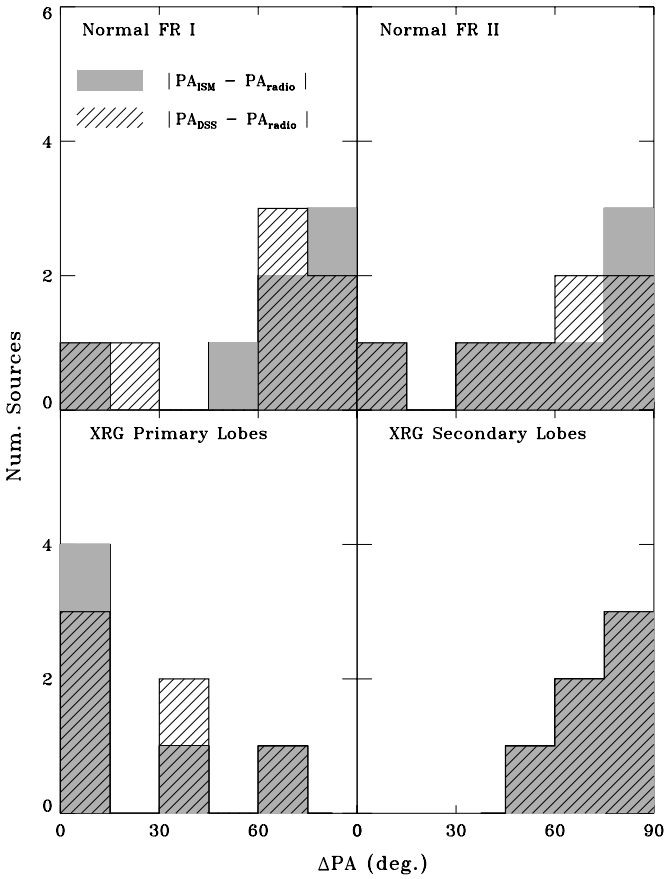

Figure 7. Comparison of the alignment of the radio jets with the interstellar medium (filled) and the optical light (hashed). ΔP.A. is the acute angle between the major axes of the best-fit ellipses (Section 3.1) and the orientation of the radio jets. ΔP.A. $\sim 0°$ indicates alignment of the *major* axis of the medium with the radio lobes, whereas ΔP.A. $\sim 90°$ indicates alignment with the *minor* axis. Note not all galaxies are represented here.

the ΔP.A. distribution for this "best guess" sample is drawn from a uniform parent is $P = 0.006$ for the primary lobes and $P = 0.001$ for the secondary ones. Regardless, the samples individually are distinguishable from normal radio galaxies by their jet—medium geometry.

Does this geometry necessarily implicate the overpressured cocoon model? NGC 326, 3C 433, and 4C +00.58 obey the C02 geometry but would be difficult to form in the overpressured cocoon model alone. NGC 326, for example, is a well studied XRG which has longer secondary lobes than primary ones. This poses a problem for the overpressured cocoon model, since we expect the jets to expand supersonically and the wings to be (at most) transonic. The long secondary lobes may therefore imply buoyant evolution of the backflow (Worrall et al. 1995), although subsonic expansion of the primary lobes is possible. 3C 433 is an especially odd case since the southern radio lobes are of qualitatively different character than the northern counterparts. Miller & Brandt (2009) argue that the difference between the northern (FR I) and southern (FR II) lobes is due to propagating into a very asymmetric medium. The secondary lobes are close to the ISM, so it is ambiguous which medium is relevant for XRG formation. Lastly, 4C +00.58 appears to violate the C02 geometry as the jet appears to come out of the minor axis of the ISM. 4C +00.58 almost certainly disagrees with the C02 geometry in the optical image (due to the high ϵ the major axis is likely to be close to the plane of the sky) and we detect an X-ray jet cospatial with the northern radio jet. However, it is

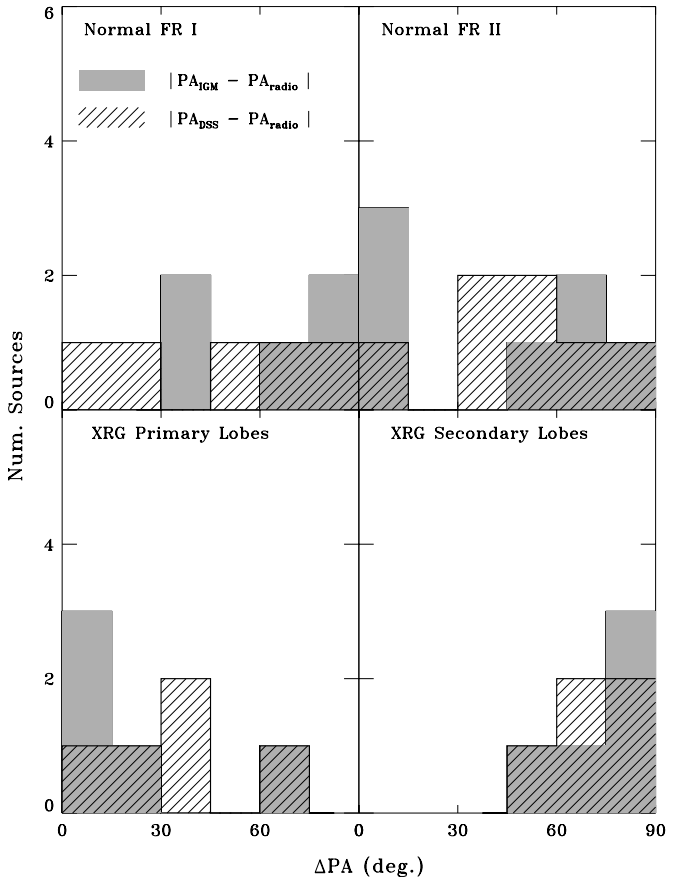

Figure 8. Comparison of the alignment of the radio jets with the local IGM (filled, see the text) and the optical light (hashed). ΔP.A. is the acute angle between the major axes of the best-fit ellipses (Section 3.1) and the orientation of the radio jets. ΔP.A. $\sim 0^\circ$ indicates alignment of the *major* axis of the medium with the radio lobes, whereas ΔP.A. $\sim 90^\circ$ indicates alignment with the *minor* axis. Not all galaxies are represented here.

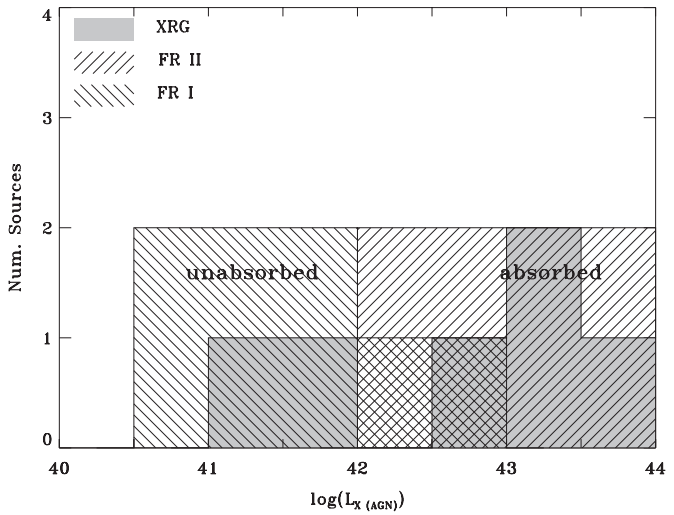

Figure 9. Distribution of the XRG and comparison sample model luminosities for spectra extracted from the central PSF. The luminosities are calculated for the full model fit. FR II galaxies tend to have highly absorbed spectra with corresponding high luminosities, whereas FR I galaxies tend to have unabsorbed spectra. XRGs have both absorbed and unabsorbed spectra.

unclear that the extended X-ray emission comes entirely from the ISM. Deeper follow-up observations are required to assess the role of the IGM in this source and establish whether it is actually a counterexample to the C02 geometry. 3C 192 is an ambiguous case because although it obeys the C02 geometry, the eccentricity of the ISM is small. For 3C 192 to be produced in the overpressured cocoon model, small differences in pressure gradients must be important.

4. PROPERTIES OF THE CENTRAL ENGINE

In the backflow models, FR II morphology is thought to be necessary to drive strong backflows. Although the backflows begin at the hot spots, edge-brightened FR II morphology is strongly associated with absorbed power-law AGN emission. We note that several galaxies in our XRG sample are not unambiguously FR type II (some of the galaxies with poor data are FR I), so we attempt to characterize the XRG sample in terms of absorbed or unabsorbed AGN spectra. Highly absorbed spectra tend to have higher L_X for a given flux than unabsorbed spectra owing to the large amount of "absorption" blocking the low-energy photons, whereas unabsorbed spectra tend to be lower energy with small X-ray luminosities above $\sim$2 keV.

Our model fitting of the AGN spectra started by fitting a single power law (either absorbed or unabsorbed depending on the appearance of the spectrum). Additional complexity was added as the degrees of freedom allowed until an acceptable fit was achieved. We note that $N_{\rm H}$ and Γ are often degenerate and require one of the two to be frozen (to values ranging from $\Gamma = 1.0$–2.0; Table 7). All the fits also incorporated Galactic $N_{\rm H}$. Our model parameters and luminosities are given in Table 7 and are largely in accordance with previous studies of the 3CRR *Chandra* sample (Evans et al. 2006; Balmaverde et al. 2006). These papers have also conducted a more exhaustive study of the AGN X-ray emission, whereas our purpose is to determine whether this emission lends insight to the XRG sample.

In fact, the XRG sample cannot neatly be classified in terms of absorbed or unabsorbed spectra (Figure 9). This is in agreement with other evidence (e.g., optical data from Cheung et al. 2009), although the highly absorbed XRGs do not tend to have a smaller L_X than the normal FR II galaxies. Indeed, the XRG sample, while small, is consistent with the distribution of L_X between 10^{40} and 10^{44} erg s^{-1} for the full comparison sample, and not with either the normal FR I or II galaxies by themselves. We note that we detect X-ray jets in some of our systems, but we find no evidence for misaligned jets in any of the XRGs. The sample size is too small to rule out the Lal & Rao (2007) model on this basis, but we might expect to see misaligned jets in their scheme.

5. DISCUSSION AND SUMMARY

We present new and archival *Chandra* data of XRGs alongside normal FR I and II galaxies within $z \leqslant 0.1$. We extend the Capetti et al. (2002) and Saripalli & Subrahmanyan (2009) geometric correlation between the orientation of the secondary lobes in XRGs and the minor axis of the interacting medium to the X-ray band, including the IGM/ICM. We find that this geometry strongly distinguishes the XRGs from normal radio galaxies (although we are unable to strongly distinguish between XRGs and normal radio galaxies using only the local IGM/ICM values), and that XRGs may be produced in galaxies with both absorbed and unabsorbed AGN. Our results in the X-ray band are consistent with Cheung et al. (2009) who find that XRGs lie close to the FR I/II division in a comparison of radio–optical luminosity. We note that in properties of the hot atmospheres (temperature, density, and pressure), the XRG sample appears

Table 7
Radio Galaxy Nuclei X-ray Spectral Parameters

Galaxy	z	Galactic N_H (10^{20} cm^{-2})	Models	Local N_H (10^{22} cm^{-2})	Γ	kT (keV)	Luminosity (10^{42} erg s^{-1})	χ^2/d.o.f
XRGs								
PKS 1422+26	0.037	1.54	N_H(PL+Gauss)	4. ± 1.	0.5 ± 0.4	...	3.8	8.2/16
NGC 326	0.048	5.86	N_H(PL)+apec	0.5 (f)	1.3 ± 0.4	0.68 ± 0.06	0.15	11.1/16
3C 403	0.059	12.2	N_H(PL+Gauss)+PL+apec	46.± 5.	$\Gamma_1 = 1.9 \pm 0.1$ $\Gamma_2 = 2.0$ (f)	0.24 ± 0.03	16.6	100.7/94
4C +00.58	0.059	7.14	PL	...	1.3 ± 0.6	...	1.1	1.6/4
3C 192	0.060	4.08	N_H(PL)	16 (f)	2.0 (f)	...	3.1	0.9/2
3C 433	0.102	7.77	N_H(PL+Gauss)+apec	8. ± 1.	1.1 ± 0.1	1.0 ± 0.2	59	72.5/77
Comparison sample								
3C 449	0.017	8.99	N_H(PL)+apec	0.5 (f)	1.6 ± 0.2	0.59 ± 0.08	0.05	7.6/14
3C 31	0.017	5.36	PL+apec	...	1.9 ± 0.1	0.70 ± 0.03	0.13	81./83
3C 83.1B	0.018	13.4	N_H(PL)+apec	2.2 ± 0.9	2.0 ± 0.3	0.48 ± 0.08	0.05	22.7/36
3C 264	0.021	1.83	PL+apec	...	2.13 ± 0.03	0.34 ± 0.06	1.7	152.7/154
3C 66B	0.022	7.67	PL+apec	...	2.17 ± 0.06	0.52 ± 0.08	0.33	90.6/114
3C 296	0.026	1.92	N_H(PL)+apec	0.10 (f)	1.1 ± 0.1	0.68 ± 0.02	0.38	91.8/81
NGC 6251	0.024	5.59	N_H(PL)+apec	0.05 ± 0.01	1.5 ± 0.03	0.35 ± 0.05	8.0	391/386
PKS 2153−69	0.028	2.67	pileup(PL)+apec	...	1.49 ± 0.05	0.4 ± 0.2	12.2	73.1/86
3C 98	0.030	10.8	N_H(PL)+gauss+PL	9. ± 1.	$\Gamma_1 = 1.2$ (f) $\Gamma_2 = 1.5$ (f)	...	3.1	47.4/35
3C 465	0.031	4.82	N_H(PL)+apec	0.3 (f)	2.4 ± 0.2	0.83 ± 0.06	0.31	62.0/62
3C 293	0.045	1.27	N_H(PL)+apec	11 ± 4	1.5 (f)	1.55 (f)	4.5	9.3/10
Cyg A	0.056	30.2	pileup(N_H(PL))+gauss+cflow	25 ± 2	2.0 (f)	...	87.6	294.3/217
3C 445	0.056	4.51	pileup(N_H(PL))+gauss[a]	16 ± 1	1.7 (f)	...	47.	62.4/44
3C 285	0.079	1.27	N_H(PL)+gauss	28 ± 4	1.2 (f)	...	8.7	12.6/9
3C 452	0.081	9.64	N_H(PL)+gauss+apec+PEXRAV[b]	38 ± 9	1.65 (f)	0.8 ± 0.2	25	156.6/145
3C 227	0.087	2.11	pileup(N_H(PL))+PL	3.3 ± 0.1	$\Gamma_1 = 1.75$ (f) $\Gamma_2 = 1.0 \pm 0.2$	...	155	248.9/167
3C 388	0.091	5.58	PL+apec	...	2.3 ± 0.3	1.2 ± 0.2	1.9	14.1/16

Notes. Reported errors for Γ are the *smaller* of the values given by 90% confidence intervals determined in XSPEC; if there is significant asymmetry about the best-fit value, the larger error bar is ill defined. (f) denotes a frozen parameter, and complex model components are discussed in theAppendix with the relevant galaxy. The "fits" to low-count spectra (e.g., 3C 192 or 4C +00.58) are not reliable, but they do constrain well whether the spectrum is absorbed or unabsorbed, so we report them only for an order-of-magnitude luminosity estimate.

[a] Complex emission between 0.5 and 3.0 keV is ignored; see the Appendix.

[b] PEXRAV is a reflection model from Magdziarz & Zdziarski (1995).

indistinguishable from the comparison sample (Table 3) but that these parameters are spatial averages of profiles and may not be directly comparable.

The remarkable geometric distinction between the normal and XRGs may be an important clue to the genesis of the secondary lobes. We cannot rigorously examine the formation models in our data, but identify potential problems for the backflow models in several galaxies. The backflow schemes naturally explain the observed geometry, but also have yet to explain other features of XRGs in detailed modeling (e.g., the flat spectral indices of the secondary lobes; Lal & Rao 2007). However, the models are presently immature: the C02 overpressured cocoon model has only been modeled in a highly elliptical two-dimensional ISM, whereas the Kraft et al. (2005) suggestion that the buoyant backflow mechanism can produce X-shaped wings in the presence of an anisotropic buoyant medium has not been modeled. Three-dimensional modeling and deeper observations of the relevant media in XRGs are required to make a convincing case for either of these models. Notably, the rapid reorientation models have yet to present a reason for the C02 correlation. Any successful model must account for it. Lastly, deeper observations of the XRGs in our sample for which no diffuse emission was detected are required. The total sample of nearby XRGs is quite small, so every member is important.

C.S.R. and E.H.-K. thank the support of the *Chandra* Guest Observer program under grant GO89109X. E.H.-K. thanks A. I. Harris for useful discussion of the ellipse-fitting method. C.C.C. was supported by an appointment to the NASA Postdoctoral Program at Goddard Space Flight Center, administered by Oak Ridge Associated Universities through a contract with NASA. This research has made use of the NASA/IPAC Extragalactic Database (NED) which is operated by the Jet Propulsion Laboratory, California Institute of Technology, under contract with the National Aeronautics and Space Administration. The Digitized Sky Surveys were produced at the Space Telescope Science Institute under U.S. Government grant NAG W-2166. The images of these surveys are based on photographic data obtained using the Oschin Schmidt Telescope on Palomar Mountain and the UK Schmidt Telescope. The plates were processed into the present compressed digital form with the permission of these institutions.

Facilities: CXO, VLA

APPENDIX

NOTES ON INDIVIDUAL GALAXIES

A.1. XRGs

B2 1040+31A ($z = 0.036$). The radio galaxy emanates from the largest galaxy in a close triple system (Fanti et al. 1977)

which itself is contained within a large region of IGM. The larger IGM is in agreement with Worrall & Birkinshaw (2000), but for the relevant medium we use a smaller region of IGM which is bright against the large region and centered on the system. In the DSS image, the host galaxy cannot be isolated from its companions, so we use the SDSS image alone. In the X-ray band, the host galaxy is bright; whether it is AGN emission is unclear based on the spectrum. Because the character of the emission does not change much outside the PSF, we assume we are seeing primarily thermal emission.

PKS 1422+26 ($z = 0.037$). This galaxy has striking wings and "warm" spots which occur about 50% of the distance between the lobe edge and the radio core. The radio galaxy defies easy FR classification and is here considered a hybrid FR I/II galaxy. Canosa et al. (1999) found radial asymmetry in the *ROSAT* image of the IGM which the *Chandra* image confirms. The radio hot spots coincide well with decrements in the X-ray image which must be cavities blown in the gas by the radio lobes. The surface brightness of the "ridge" this leaves in the middle is consistent with the hypothesis that the actual orientation of the IGM is elongated in the direction of the radio lobes. This is in contrast to 3C 285 or 3C 388, where cavities alone cannot explain the "excess" emission near the core. In addition, the spectrum of the AGN has a highly significant emission line-like feature at 4.0 keV which is presently unexplained.

NGC 326 ($z = 0.048$). NGC 326 is a double galaxy with the radio lobes emanating from the northern component; both galaxies show diffuse X-ray ISM emission, and the X-ray emission from the southern galaxy is exclusively thermal. The extent of the *Chandra* diffuse emission agrees well with the *ROSAT* data where there is overlap (Worrall et al. 1995). The long tails in the radio map appear to follow empty channels in the *Chandra* data, and the length of the tails relative to the active lobes provides constraints on backflow formation mechanisms (Gopal-Krishna et al. 2003). The ISM emission for the northern component is extracted excluding the central point source; the temperature of $kT = 0.68$ keV agrees precisely with the temperature of the thermal model included in the AGN emission, where a PL component is also required.

3C 403 ($z = 0.059$). This data set was previously studied in detail by Kraft et al. (2005) who attempted to isolate the ISM emission from the nucleus by performing a spectral analysis in which the soft part of the spectrum was fitted by an absorbed power law between 1.0 and 2.0 keV, with a line-dominated thermal fit between 0.3 and 1.0 keV. They then fit an elliptical profile to these thermal events. This line of reasoning is supported by the absence of a bright core corresponding to the PSF at 0.3–1.0 keV. However, we find an acceptable fit in which an unabsorbed power law dominates between 0.3 and 2.0 keV. This analysis is also complicated by the presence of a feature at 0.85 keV which is not fit by either Kraft et al. (2005) or ourselves. Since this feature accounts for ∼25% of counts between 0.3 and 1.0 keV (Figure 5; we cannot distinguish between the thermal and power-law models). It should be noted that the P.A. of the soft emission agrees well with the host galaxy; we are doubtless seeing *some* ISM. However, we do not know if it is the dominant component.

4C +00.58 ($z = 0.059$). 4C +00.58 was classified as a candidate XRG (Cheung 2007) due to faint wings in the FIRST image. A new, higher resolution radio map reveals that the jet to the east of the core is bent toward the northwest and enclosed in a more symmetric radio lobe. We detect the inner part of this jet in the X-ray band (confirmed by line-fitting to determine the P.A. using the bootstrap resampling method). The P.A. of the jet was determined very well, so we masked it from our fit. It is unclear whether the diffuse emission represents the ISM or the IGM. $\epsilon_{\rm X\text{-}ray}$ does not agree well with the host galaxy, but the P.A. does. There is likely some of both media represented in the image, and deeper observations are required to separate the components. Notably, the jet appears to pass through the *minor* axis of the host galaxy. We include this galaxy in both the ISM and IGM X-ray–radio comparisons due to the ambiguity.

3C 192 ($z = 0.060$). 3C 192 is formally a "winged" galaxy (Cheung 2007), but the morphology is otherwise very similar to XRGs. Enhanced emission is detected in an elliptical region encompassing the primary radio lobes, but a smaller enhancement we identify with the ISM exists near the AGN. It is also possible that this is the central region of the IGM, but it appears compact. Moreover, the "IGM" is consistent with being fit only by a power law ($\Gamma = 2.5$) and is in good spatial agreement with the primary lobes. It may also be fitted by a thermal model with $kT \sim 0.9$ and $Z < 0.1$; if it is indeed thermal emission, the IGM is in perfect agreement with Capetti et al. (2002). However, a close inspection of the radio galaxy suggests that the X-ray emission may come from a bounding shock or otherwise have been influenced by the radio galaxy rather than a pre-existing highly eccentric IGM. In particular, even though the bright X-ray emission is not as large as the active lobes, the southwestern lobe appears to track enhanced X-ray emission to its hot spot. Notably, 3C 192 is in a very round host (Smith & Heckman 1989; Cheung & Springmann 2007). Capetti et al. (2002) found XRGs typically occur in galaxies with high projected ϵ, so the existence of similar morphology in round hosts bears investigation.

3C 433 ($z = 0.102$). The northern secondary lobe of 3C 433 is strikingly bent compared to the southern secondary (van Breugel et al. 1983). Miller & Brandt (2009) argue that the hybrid FR I/II lobe morphology is due to interaction with the surrounding IGM. In this scenario, the galaxy is a typical FR II source propagating into a very asymmetric environment. Miller & Brandt (2009) also include in their paper a *HST* image of the host galaxy whose P.A. is in good agreement with the parameters we derive from the DSS image. The X-ray emission near the southern lobe is consistent with either thermal emission (Miller & Brandt 2009) or power-law emission. We assume the ISM is the relevant medium and attempt to isolate it, but we may also be incorporating some local IGM emission in the spectrum.

3C 315 ($z = 0.108$). The AGN is detected at a significance of 5.07σ (see Appendix A.3 for methods), but there are too few counts to make a spectrum. The diffuse IGM stands out against the background on large scales and is fitted well by thermal models and not by power-law models. No ISM is detected, but we can use the galaxy for comparison to the IGM independently. It is possible that this is not real IGM, as we suspect in 3C 192, but the alignment of the radio galaxy and the hot atmosphere is not as good as in 3C 192, nor is it quite as eccentric. Thus, there is no strong evidence that the radio galaxy created the observed X-ray morphology, but the exposure is very short.

A.2. Comparison Sample

3C 449 ($z = 0.017$). Both the ISM and IGM are bright in this 30 ks exposure, but the chip is somewhat smaller than the extent of the radio lobes. Notably, these lobes decollimate and show the characteristic FR I plumed structure near the edge of the IGM; this structure and the hot atmospheres have been studied

with *XMM-Newton* in detail by Croston et al. (2003). Tremblay et al. (2007) find that the jet is parallel to a warped nuclear disk. The AGN was fitted with the XSPEC models $N_{\rm H}$(PL)+apec, but the an acceptable fit was also found for a PL+apec fit with no absorption and a smaller Γ.

3C 31 ($z = 0.017$). The X-ray jet (Hardcastle et al. 2002) is quite bright in the ACIS-S3 image and is readily distinguishable from other core X-ray emission, so we mask it in the analysis of the diffuse ISM. A weaker, nearby source to the southwest (visible in the optical light) may contaminate the ISM with a small amount of diffuse emission, but appears very weak in the X-ray.

3C 83.1B ($z = 0.018$). The *Chandra* data from this head–tail galaxy was published by Sun et al. (2005) who argue that there is a distinct southern edge to the X-ray emission which otherwise shares the ellipticity and P.A. of the optical isophotes. They apply a deprojection analysis to the ISM data and find that the central ISM has a temperature of $kT = 0.45$ keV, in agreement with our non-deprojected fit to the central PSF emission with $kT = 0.48$ keV. Sun et al. (2005) also find that the LMXB contribution to the diffuse gas is on the order of ∼5% and they show that the southern edge in the X-ray data cannot be produced by ICM pressure, but argue that the edge is a sign of ISM/ICM interaction and that if the galaxy is moving south very rapidly, the long twin tails to the north are naturally explained. The radio emission is likewise curtailed to the south.

3C 264 ($z = 0.021$). 3C 264 is a head–tail galaxy whose radio lobes both extend to the northeast, but there is a large envelope of radio emission around the AGN which is larger than the extent of the $2\sigma_{\rm sky}$ DSS optical isophotes. This data set is subarrayed to 1/8 of the ACIS-S3 area and suffers from a readout streak. We subtracted the streak and this removed a relatively small number of photons from the diffuse ISM. Both the host galaxy and the diffuse X-ray emission appear almost circular on the sky such that the P.A. of the ellipses we fit (Table 5) are not well constrained.

3C 66B ($z = 0.022$). We detect strong ISM emission and the X-ray jet in this *Chandra* exposure. The IGM is detected and studied (with regards to its interaction with the radio lobes) using *XMM-Newton* data by Croston et al. (2003). In the *Chandra* exposure, however, the IGM is very weak and we cannot measure the morphology. The different character of the two lobes is attributed to interaction with the hot gas by Croston et al. (2003), with the western lobe being more confined. There is a small unresolved source to the southeast in the X-ray image which has an optical counterpart, but it is far enough from the ISM emission that our ellipse fitting is unaffected.

3C 296 ($z = 0.024$). Before fitting an ellipse we subtract a small companion to the northwest as well as the X-ray jet. The ISM is clearly detected (see also Diehl & Statler 2007, NGC 5532 in their paper) and the lobes begin expanding outside the IGM. The IGM has a similar shape and orientation to the ISM, but it is clearly distinct in temperature and where it is centered (in between 3C 296 and a companion to the southwest) even though it is relatively compact.

NGC 6251 ($z = 0.024$). The very large (Mpc-scale) radio lobes of this radio galaxy dwarf the entire ACIS array, and the 1/8 size S3 subarray contains emission only from the central core and along the jet (Evans et al. 2005). We detect some emission associated with the jet to the northwest of the galaxy along the chip. A bright readout streak has been removed, and we correct the spectrum of the central PSF for pileup. The spectrum of the AGN is fitted well by either a power law with $\Gamma < 0.5$ and a thermal model or a slightly absorbed power law with $\Gamma = 1.5$ and a thermal model.

PKS 2153−69 ($z = 0.028$). This data have been published before with regard to interaction of the radio jet with a cloud of gas (Ly et al. 2005; Young et al. 2005). The gross morphology agrees well with the C02 geometric relation, although the surface brightness decrement to the north and south of the galaxy is due to the cavities blown out by the radio lobes, as is evident from the visible shocked bubbles of gas in the IGM. Despite these cavities, the morphology of the larger IGM is easily measurable on larger scales, assuming the internal structure is entirely due to the radio galaxy activity.

3C 338 ($z = 0.030$). Unlike other extended sources for which deprojection is possible but which can be fitted by an isothermal model to find an average temperature (most of the other galaxies in our sample), 3C 338 has sufficient signal to require at least a 2-T model to find average temperatures (signifying the presence of hotter and cooler gas) and these temperatures are roughly in line with the outer and inner temperatures of the Johnstone et al. (2002) deprojection analysis which also agrees with our own (we report the 2-T fit for consistency). Although the cluster gas is interacting with the radio galaxy, it is otherwise smooth and we take it to be a single large ellipsoid for the purpose of measuring ellipticity and P.A. of the ICM. Notably, we do not detect the AGN or the ISM amidst the very bright ICM. This observation is studied more thoroughly in Johnstone et al. (2002), including the unusual radio bridge parallel to the jets.

3C 98 ($z = 0.030$). The ISM of the galaxy in this ACIS-I observation is very close to the chip boundaries. However, it has clear ellipticity and is not contaminated by any companions, so we are able to fit an ellipse. There is diffuse thermal emission associated with the northern radio lobe that is similar to the ISM, but we see no evidence for such gas in the southern lobe. Notably, the orientation of the major axis of the *HST* image in Martel et al. (1999) disagrees with our DSS ellipse by ∼20°. The *HST* image is more reliable, meaning that the radio jet is aligned close to the *major* axis of the host.

3C 465 ($z = 0.031$). 3C 465 is a wide-angle tail FR I radio galaxy located in cluster gas that has been well studied (both with *Chandra* and *XMM-Newton* by Hardcastle et al. 2005). The ICM covers most of the chip and is centered on the host of 3C 465. The ICM has clear ellipticity and the bright extended emission is comparable to the size of entire radio galaxy. We fit ellipses to both the ISM and "local" ICM on a scale slightly smaller than half the size of the chip. Hardcastle et al. (2005) also present a radial profile which is in agreement with our average temperature for the cluster gas. The spectrum of the AGN can be fitted well either by a power law with $\Gamma < 0.5$ and a thermal model or a slightly absorbed power law with $\Gamma = 2.4$ and a thermal model.

3C 293 ($z = 0.045$). The X-ray emission associated with the radio galaxy is quite weak, but the hot spots are distinct and there is a small amount of extended ISM emission. Unfortunately, the spatial extent of this diffuse emission is small compared to the optical isophotes, so the disagreement between the $\epsilon_{\rm X\text{-}ray}$ and $\epsilon_{\rm DSS/SDSS}$ (measured at a somewhat larger radius) is not especially surprising. Notably, the host galaxy has two nuclei and is in the process of merging (Martel et al. 1999).

Cyg A ($z = 0.056$). Cygnus A has been extensively studied in the X-rays thanks to its exceptionally bright filamentary structure and evident shock cocoon tracing the radio galaxy. This structure makes it impossible to measure the ellipse parameters of the ISM, but the larger ICM appears to have little structure

beyond the cocoon and filaments (Young et al. 2002, show that the host galaxy has complex morphology as well). Therefore, we believe the directions of pressure and density gradients on large scales are likely to be similar to the ones the radio galaxy encounters.

3C 445 ($z = 0.056$). The bright nucleus of 3C 445 is far off-axis in this exposure; its brightness and high ellipticity make it impossible to measure the ellipse parameters of the diffuse ISM. Moreover, the Martel et al. (1999) *HST* image is dominated by the unresolved nucleus, so our DSS parameters may not be accurate. However, we include the galaxy in our sample because of the hot IGM surrounding the host.

3C 285 ($z = 0.079$). 3C 285 is currently experiencing a major merger, and instead of a well defined ISM, we fit an ellipse to the "ridge" structure described in Hardcastle et al. (2007b). The ridge appears to be a unified structure (its X-ray properties do not differ along its length) and Hardcastle et al. (2007b) argue that it is *not* produced by the interaction of the radio galaxy with its environment. They reason that the agreement with the starlight (and, in 3C 442A, the flow of material from tidal tails into a similar ridge) could not be generally predicted by the interaction of the radio galaxy with its environment. This is in agreement with our ISM–optical light correlation.

3C 452 ($z = 0.081$). This data set was studied in detail by Isobe et al. (2002) who find that the thermal and power-law emission is well mixed throughout the region covered by the radio lobes. We attempt to isolate the two components using an analysis similar to Diehl & Statler (2007) in which the image is broken into hard and soft components. The thermal and power-law emission each make up a certain percentage of the luminosity in each component, so a synthesized image of the thermal emission can be constructed by adding the correct percentage of each component to the final image. Although clearly the method will not be able to identify individual counts as thermal or nonthermal in origin, if the spatial distribution of nonthermal counts is significantly different from that of thermal ones, we would expect to see a difference in the synthesized images. In fact, we find general agreement with Isobe et al. (2002), although the nonthermal emission is dominant near the hot spots of the radio galaxy. If the thermal X-ray emission traces the physical boundaries of the IGM, then we would expect to see either an X- or Z-shaped galaxy, but the extremely good coincidence between X-ray and radio emission argues that this is instead a cocoon inside a larger (unseen) IGM.

3C 227 ($z = 0.087$). 3C 227 exhibits both core ISM and dimmer IGM emission near the host galaxy. The IGM morphology is difficult to study due to the chip boundary. The radio lobes appear to be ragged and bend around the major axis of the host galaxy, suggesting that strong backflows similar to those in the hydrodynamic XRG formation models are at work, but the IGM is too weak near these mini-wings to assess this hypothesis. The galaxy was included in the Hardcastle et al. (2007a) study of particle acceleration in hot spots.

3C 388 ($z = 0.091$). 3C 388 is a radio galaxy oriented along the major axis of its host, but we detect no ISM in the X-ray exposure due to the strength of the surrounding ICM. The radio galaxy is comparable to the size of X-ray ICM isophotes elongated in its direction, which Kraft et al. (2006) attribute to the influence of the radio galaxy on its surroundings. The radio lobes have blown cavities in the X-ray emission, but near the core of the radio galaxy, the X-ray isophotes are elongated in a direction perpendicular to the radio lobes. Although much of this asymmetry is likely due to the cavities eating out the sides of a spheroid where the radio galaxy overlaps the core region (i.e., it is a physical structure but may not precede the radio galaxy), the western radio lobe seems to bend around the ridge. Since the fainter portions of the radio lobes may be older plasma evolving buoyantly in the ICM (the jet in the western lobe is farther to the south), the ridge may also be influencing the shape of the radio galaxy.

A.3. Unused XRGs

Short observations of the more distant XRGs produced mixed results, with a number of sources exhibiting little-to-no diffuse emission. Where we cannot determine whether any diffuse emission is dominated by thermal emission or measure morphology, or where no diffuse emission corresponding to the relevant medium is detected, we cannot use the galaxy in our analysis. In the following short observations, the central point source is detected in all cases (with the weakest detection having a significance barely exceeding 3σ), and upper limits are given for the thermal luminosity. We use the methods of Ayres (2004, Equations (3), (13), and (14) in his paper) to measure the detection significance and flux confidence limits. The measured number of counts is given by

$$S = S_0 + \left(\frac{s^2+2}{3}\right) \pm \Delta S,$$

where $S_0 = N - B$ is the detected number of counts in the cell, B is the expected background in the cell based on a much larger area elsewhere on the chip, and s is the significance; we choose $s = 1.645$ for 95% confidence intervals. The quantity ΔS is given by

$$\Delta S \equiv s\sqrt{\max[(N - \tfrac{1}{4}B), 0] + 1}.$$

The detect cells we used were uniformly chosen to be circles with $3''$ in radius to enclose the *Chandra* PSF at most energies. The significance of the detection s was determined by solving the quadratic equation (Equation (3) in Ayres 2004):

$$\frac{\min[B^{0.1}, 1]}{7}s^2 + \sqrt{B}s + \left[B - N - \frac{2 \cdot \min[B^{0.1}, 1]}{7}\right] = 0.$$

These values are reported for each galaxy. The thermal luminosity upper limits were computed by extracting a spectrum from a (large) region around the point source and increasing the strength of a thermal model in XSPEC until it was no longer a good fit. The temperature cannot be constrained and was thus fixed at $kT = 1.0$ keV. The unabsorbed luminosity was then computed at the upper bound of the model normalization and reported below.

4C + 32.25 ($z = 0.053$). The point source is detected with a significance of 8.52σ with $S = 20.7^{+9.4}_{-6.3}$ counts in the detect cell. The diffuse emission within a $r = 24''$ region (much larger than the ISM) has an upper limit unabsorbed thermal luminosity of 4×10^{40} erg s^{-1} at ~1.0 keV, but it does not appear to be centrally concentrated on the chip. Our geometric analysis is not possible in this case, especially since the ISM is the medium of interest given the scale of the radio emission.

4C + 48.29 ($z = 0.052$). We detect 19 counts in the detect cell (positioned around the core of radio emission) and detect the AGN with a significance of 7.56σ and $S = 17.6^{+8.9}_{-5.7}$ counts in a 95% confidence interval. The diffuse emission in a $r = 24''$ region is barely distinguishable from the background

and we measure an unabsorbed thermal luminosity upper limit of $L = 5 \times 10^{40}$ erg s^{-1}. We attribute this to the faint IGM as opposed to the ISM due to the scale and lack of central concentration.

3C 136.1 ($z = 0.064$). This source has relatively high background, so we detect the AGN at a significance of only 3.3σ despite finding 11 counts in the detect cell. The number of counts is $S = 7.9^{+7.1}_{-3.9}$. Any diffuse emission is similarly buried in the background, and we measure an unabsorbed thermal luminosity upper limit of $L = 2 \times 10^{40}$ erg s^{-1} for a region with $r = 30''$.

J1101+1640 ($z = 0.068$). Unfortunately, this XRG was not positioned on any ACIS chip during the observation. The galaxy lies in a cluster (Abell 1145) and the radio lobes just extend onto part of the S3 chip, but no significant diffuse gas from the cluster is detected on the chip. The observation was mispointed due to an error in the primary literature and so cannot be used.

3C 223.1 ($z = 0.107$). 3C 223.1 actually has a bright AGN core where spectroscopy is possible, revealing a highly absorbed power law. The detection significance is 34.1σ and the number of counts detected $S = 206^{+25}_{-22}$. However, any diffuse emission is extremely faint, with an upper limit to unabsorbed thermal luminosity of $L = 8 \times 10^{40}$ erg s^{-1} in a region with $r = 30''$. We are therefore unable to use this galaxy in our XRG sample.

We also choose not to use the two *Chandra* observations of XRGs at higher redshift ($z = 0.128, 0.2854$) because of the requirement to simultaneously expand the comparison sample (and 3C 197.1 is not included in the compilation of Cheung 2007). We address these here as follows.

3C 197.1 ($z = 0.128$). 3C 197.1 has a long northern wing which is comparable in spatial extent to the active lobe in a 1.5 GHz image (Neff et al. 1995), but there is no obvious southern wing which could be described as symmetric about the central AGN. In the 5 GHz image of Neff et al. (1995) extensions in the southern lobe appear to be essentially symmetric about the jet axis. 3C 197.1 is included in the Saripalli & Subrahmanyan (2009) list of XRGs, but its inclusion in our sample is questionable. We discuss it here because of the other "XRGs" listed in Saripalli & Subrahmanyan (2009) and not in Cheung (2007), 3C 197.1 bears the most similarity to the classical XRGs listed in Cheung (2007). We do not include it in our sample due to its relatively high redshift and ambiguity of classification. The *Chandra* exposure is a short 8 ks snapshot which clearly detects the AGN and some diffuse emission which may be the ISM or the IGM, but has insufficient counts to claim a spectroscopic detection of hot gas.

3C 52 ($z = 0.285$). 3C 52 is a classical XRG with highly collimated secondary lobes in the 1.5 GHz image (Alexander & Leahy 1987) and excluded from our sample on the basis of much higher redshift than our other sources. The *Chandra* image is an 8 ks snapshot which clearly detects the central point source and also a diffuse atmosphere larger than the radio galaxy itself (with a radius of about 50 arcsec centered on the galaxy). This atmosphere is in good agreement geometrically with the Capetti et al. (2002) relation (i.e., the major axis of the ellipsoidal atmosphere is co-aligned with the active lobes), but proving the presence of a hot atmosphere spectroscopically is difficult. An isothermal `apec` model requires $T > 7$ keV and is otherwise poorly constrained; a power law with $\Gamma = 1.5$ fits the spectrum well. Since the emission region is large compared to the radio galaxy, it seems likely this is hot gas, but a much deeper observation is necessary to establish this.

REFERENCES

Adelman-McCarthy, J., et al. 2008, ApJS, 175, 297
Alexander, P., & Leahy, J. P. 1987, MNRAS, 225, 1
Arnaud, K. A. 1996, in ASP. Conf. Ser. 101, Astronomical Data Analysis Software and Systems V, ed. G. H. Jacoby & J. Barnes (San Francisco, CA: ASP), 17
Ayres, T. R. 2004, ApJ, 608, 957
Balmaverde, B., Capetti, A., & Grandi, P. 2006, A&A, 451, 35
Baum, S. A., Heckman, T., Bridle, A., van Breugel, W., & Miley, G. 1988, ApJS, 68, 643
Becker, R. H., White, R. L., & Helfand, D. J. 1995, ApJ, 450, 559
Binney, J., & Merrifield, M. 1998, Galactic Astronomy (Princeton Series in Astrophysics; Princeton, NJ: Princeton Univ. Press)
Black, A. R. S., Baum, S. A., Leahy, J. P., Perley, R. A., Riley, J. M., & Scheuer, P. A. G. 1992, MNRAS, 256, 186
Bogdanović, T., Reynolds, C. S., & Miller, M. C. 2007, ApJ, 661, L147
Canosa, C. M., Worrall, D. M., Hardcastle, M. J., & Birkinshaw, M. 1999, MNRAS, 310, 30
Capetti, A., Zamfir, S., Rossi, P., Bodo, G., Zanni, C., & Massaglia, S. 2002, A&A, 394, 39
Cheung, C. C. 2007, AJ, 133, 2097
Cheung, C. C., Healey, S. E., Landt, H., Kleijn, G. V., & Jordán, A. 2009, ApJS, 181, 548
Cheung, C. C., & Springmann, A. 2007, in ASP Conf. Ser. 373, The Central Engine of Active Galactic Nuclei, ed. L. C. Ho & J.-M. Wang (San Francisco, CA: ASP), 259
Condon, J. J., Frayer, D. T., & Broderick, J. J. 1991, AJ, 101, 362
Croston, J. H., Hardcastle, M. J., Birkinshaw, M., & Worrall, D. M. 2003, MNRAS, 346, 1041
Dennett-Thorpe, J., Scheuer, P. A. G., Laing, R. A., Bridle, A. H., Pooley, G. G., & Reich, W. 2002, MNRAS, 330, 609
Diehl, S., & Statler, T. 2007, ApJ, 668, 150
Donato, D., Sambruna, R. M., & Gliozzi, M. 2004, ApJ, 617, 915
Efron, B. 1982, CBMS-NSF Regional Conf. Ser. in Applied Mathematics, The Jackknife, the Bootstrap and Other Resampling Plans (Philadelphia, PA: Soc. for Industrial & Applied Mathematics)
Ekers, R. D., Fanti, R., Lari, C., & Parma, P. 1978, Nature, 276, 588
Evans, D. A., Hardcastle, M. J., Croston, J. H., Worrall, D. M., & Birkinshaw, M. 2005, MNRAS, 359, 363
Evans, D. A., Worrall, D. M., Hardcastle, M. J., Kraft, R. P., & Birkinshaw, M. 2006, ApJ, 642, 96
Fanaroff, B. L., & Riley, J. M. 1974, MNRAS, 167, 31P
Fanti, C., Fanti, R., Gioia, I. M., Lari, C., Parma, P., & Ulrich, M.-H. 1977, A&AS, 29, 279
Fosbury, R. A. E., Morganti, R., Wilson, W, Ekers, R. D., di Serego Alighieri, S., & Tadhunter, C. N. 1998, MNRAS, 296, 701
Ge, J., & Owen, F. N. 1994, AJ, 108, 1523
Gopal-Krishna, Biermann, P. L., & Wiita, P. J. 2003, ApJ, 594, L103
Gopal-Krishna, & Wiita, P. J. 2000, A&A, 363, 507
Hardcastle, M. J., Alexander, P., Pooley, G. G., & Riley, J. M. 1996, MNRAS, 278, 273
Hardcastle, M. J., Birkinshaw, M., & Worrall, D. M. 2001, MNRAS, 326, 1499
Hardcastle, M. J., Croston, J. H., & Kraft, R. P. 2007a, ApJ, 669, 893
Hardcastle, M. J., Evans, D. A., & Croston, J. H. 2006, MNRAS, 370, 1893
Hardcastle, M. J., Harris, D. E., Worrall, D. M., & Birkinshaw, M. 2004, ApJ, 612, 729
Hardcastle, M. J., Kraft, R. P., Worrall, D. M., Croston, J. H., Evans, D. A., Birkinshaw, M., & Murray, S. S. 2007b, ApJ, 662, 166
Hardcastle, M. J., Sakelliou, I., & Worrall, D. M. 2005, MNRAS, 359, 1007
Hardcastle, M. J., Worrall, D. M., Birkinshaw, M., Laing, R. A., & Bridle, A. H. 2002, MNRAS, 334, 182
Isobe, N., Tashiro, M., Makishima, K., Iyomoto, N., Suzuki, M., Murakami, M. M., Mori, M., & Abe, K. 2002, ApJ, 580, L111
Jeltema, T. E., Binder, B., & Mulchaey, J. S. 2008, ApJ, 679, 1162
Johnstone, R. M., Allen, S. W., Fabian, A. C., & Sanders, J. S. 2002, MNRAS, 336, 299
Kalberla, P. M. W., Burton, W. B., Hartmann, D., Arnal, E. M., Bajaja, E., Morras, R., & Pöppel, W. G. L. 2005, A&A, 440, 775
Klein, U., Mack, K.-H., Gregorini, L., & Parma, P. 1995, A&A, 303, 427
Kraft, R. P., Azcona, J., Forman, W. R., Hardcastle, M. J., Jones, C., & Murray, S. S. 2006, ApJ, 639, 753
Kraft, R. P., Hardcastle, M. J., Worrall, D. M., & Murray, S. S. 2005, ApJ, 622, 149
Laing, R. A., Riley, J. M., & Longair, M. S. 1983, MNRAS, 204, 151
Lal, D. V., & Rao, A. P. 2007, MNRAS, 374, 1085
Lambas, D. G., Maddox, S. J., & Loveday, J. 1992, MNRAS, 258, 404

Leahy, J. P., Black, A. R. S., Dennett-Thorpe, J., Hardcastle, M. J., Komissarov, S., Perley, R. A., Riley, J. M., & Scheuer, P. A. G. 1997, MNRAS, 291, 20
Leahy, J. P., & Perley, R. A. 1991, AJ, 102, 537
Leahy, J. P., & Parma, P. 1992, in Extragalactic Radio Sources: From Beams to Jets, ed. J. Roland, H. Sol, & G. Pelletier (Cambridge: Cambridge Univ. Press), 307
Leahy, J. P., & Williams, A. G. 1984, MNRAS, 210, 929
Ly, C., de Young, D. S., & Bechtold, J. 2005, ApJ, 618, 609
Magdziarz, P., & Zdziarski, A. A. 1995, MNRAS, 273, 837
Martel, A. R., et al. 1999, ApJS, 122, 81
Massaro, F., et al. 2008, AAS HEAD meeting #10, 26.19
Merritt, D., & Ekers, R. D. 2002, Science, 297, 1310
Miller, B. P., & Brandt, W. N. 2009, ApJ, 695, 755
Murgia, M., Parma, P., de Ruiter, H. R., Bondi, M., Ekers, R. D., Fanti, R., & Fomalont, E. B. 2001, A&A, 380, 102
Neff, S. G., Roberts, L., & Hutchings, J. B. 1995, ApJS, 99, 349
Perley, R. A., Dreher, J. W., & Cowan, J. J. 1984, ApJ, 285, L35
Perlman, E. S., Georganopoulos, M., May, E. M., & Kazanas, D. 2010, ApJ, 708, 1
Press, W. H., Teukolsky, S. A., Vetterling, W. T., & Flannery, B. P. 1992, Numerical Recipes in C: The Art of Scientific Computing (2nd ed.; Cambridge: Cambridge Univ. Press)
Rees, M. 1978, Nature, 275, 516
Reynolds, C. S., Heinz, S., & Begelman, M. C. 2001, ApJ, 549, L179
Roettiger, K., Burns, J., Clarke, D. A., & Christiansen, W. A. 1994, ApJ, 421, L23
Rottmann, H. 2001, PhD thesis, Univ. Bonn
Sambruna, R. M., Gliozzi, M., Donato, D., Tavecchio, F., Cheung, C. C., & Mushotzky, R. F. 2004, A&A, 414, 885
Saripalli, L., & Subrahmanyan, R. 2009, ApJ, 695, 156
Smith, E. P., & Heckman, T. M. 1989, ApJ, 341, 685
Smith, D. A., Wilson, A. S., Arnaud, K. A., Terashima, Y., & Young, A. J. 2002, ApJ, 565, 195
Sun, M., Jerius, D., & Jones, C. 2005, ApJ, 633, 165
Sun, M., Voit, G. M., Donahue, M., Jones, C., Forman, W., & Vikhlinin, A. 2009, ApJ, 693, 1142
Thompson, A. R., Clark, B. G., Wade, C. M., & Napier, P. J. 1980, ApJS, 44, 151
Tremblay, G. R., Chiaberge, M., Donzelli, C. J., Quillen, A. C., Capetti, A. Sparks, W. B., & Maccheto, F. D. 2007, ApJ, 666, 109
van Breugel, W., Balick, B., Heckman, T., Miley, G., & Helfand, D. 1983, AJ, 88, 1
Wirth, A., Smarr, L., & Gallagher, J. S. 1982, AJ, 87, 602
Worrall, D. M., & Birkinshaw, M. 2000, ApJ, 530, 719
Worrall, D. M., Birkinshaw, M., & Cameron, R. A. 1995, ApJ, 449, 93
Wright, E. L. 2006, PASP, 118, 1711
Young, A. J., Wilson, A. S., Terashima, Y., Arnaud, K. A., & Smith, D. A. 2002, ApJ, 564, 176
Young, A. J., Wilson, A. S., Tingay, S. J., & Heinz, S. 2005, ApJ, 622, 830
Zier, C. 2005, MNRAS, 364, 583
Zier, C., & Biermann, P. L. 2001, A&A, 377, 23